

INVESTIGATION OF STRUCTURAL PROPERTIES OF METAL NANORODS:  
MOLECULAR DYNAMICS SIMULATIONS

A THESIS SUBMITTED TO  
THE GRADUATE SCHOOL OF NATURAL AND APPLIED SCIENCES  
OF  
MIDDLE EAST TECHNICAL UNIVERSITY

HÜSEYİN YAĞLI

IN PARTIAL FULFILLMENT OF THE REQUIREMENTS  
FOR  
THE DEGREE OF MASTER OF SCIENCE  
IN  
MICRO AND NANOTECHNOLOGY

JULY 2014



Approval of the thesis:

**INVESTIGATION OF STRUCTURAL PROPERTIES OF METAL  
NANORODS: MOLECULAR DYNAMICS SIMULATIONS**

submitted by **HÜSEYİN YAĞLI** in partial fulfillment of the requirements for the degree of **Master of Science in Micro and Nanotechnology Department, Middle East Technical University** by,

Prof. Dr. Canan Özgen  
Dean, Graduate School of Natural and Applied Sciences

\_\_\_\_\_

Prof. Dr. Tayfun Akın  
Head of Department, **Micro and Nanotechnology**

\_\_\_\_\_

Prof. Dr. Şakir Erkoç  
Supervisor, **Physics Dept., METU**

\_\_\_\_\_

Assist. Prof. Dr. Yiğit Yazıcıoğlu  
Co-Supervisor, **Mechanical Engineering Dept., METU**

\_\_\_\_\_

**Examining Committee Members:**

Prof. Dr. Ümit Kızıloğlu  
Physics Dept., METU

\_\_\_\_\_

Prof. Dr. Şakir Erkoç  
Physics Dept., METU

\_\_\_\_\_

Prof. Dr. Amdulla Mekrbov  
Metallurgical and Materials Engineering Dept., METU

\_\_\_\_\_

Prof. Dr. Mehmet Şimşek  
Physics Dept., Gazi University

\_\_\_\_\_

Assoc. Prof. Dr. Hüseyin Oymak  
Physics Group, Atılım University

\_\_\_\_\_

Date 22/07/2014

**I hereby declare that all information in this document has been obtained and presented in accordance with academic rules and ethical conduct. I also declare that, as required by these rules and conduct, I have fully cited and referenced all material and results that are not original to this work.**

Name, Last name: Hüseyin YAĞLI

Signature :

# ABSTRACT

## INVESTIGATION OF STRUCTURAL PROPERTIES OF METAL NANORODS: MOLECULAR DYNAMICS SIMULATIONS

YAĞLI, Hüseyin

M.Sc., Department of Micro and Nanotechnology

Supervisor: Prof. Dr. Şakir ERKOÇ

Co-Supervisor: Assist. Prof. Dr. Yiğit YAZICIOĞLU

July 2014, 83 pages

After recent advances in microscopy and characterization techniques reached smaller length scales down to individual atoms, nanowires attracted a large interest. The material properties that are not changeable in bulk materials can be controlled in nanowires to fit the requirements of the intended application area. Characterization of nanowires is important in order to establish a reproducible relationship with their characteristics and their desired functionality.

In this thesis, structural properties of copper, silver and gold nanowires with three different widths generated from low-index surfaces (100), (110), (111) under strain have been investigated. Classical molecular dynamics simulations have been performed at 1 K and 300 K using an atomistic potential consisting of two body interactions among the atoms. Strain has been applied to the nanowires along the uniaxial wire direction. It has been found that uniaxial strain shows cross section geometry and temperature dependent characteristics. The nanowires generated from (100) and (110) surfaces are relatively stronger against uniaxial strain than the nanowires generated from (111) surface. Temperature has a positive effect to the ductility of the nanowires. The nanowires could not form 1-D structures without fragmentation.

Keywords: Molecular Dynamics Simulations, Copper Nanowires, Silver Nanowires, Gold Nanowires, Strain

# ÖZ

## METAL NANOÇUBUKLARIN YAPI ÖZELLİKLERİNİN İNCELENMESİ: MOLEKÜL DİNAMIĞI BENZETİŞİMLERİ

YAĞLI, Hüseyin

Yüksek Lisans, Mikro ve Nanoteknolojiler Bölümü

Tez Yöneticisi: Prof. Dr. Şakir ERKOÇ

Ortak Tez Yöneticisi: Yard. Doç. Dr. Yiğit YAZICIOĞLU

Temmuz 2014, 83 sayfa

Yakın geçmişte yaşanan mikroskopi ve karakterizasyon tekniklerindeki ilerlemelerin tek atom boyutlarına inen ölçeklere ulaşması sonucu nanoteller geniş bir ilgi odağı haline gelmiştir. İri hacimli (bulk) iken değiştirilemeyen bazı malzeme özellikleri nanotellerde kontrol edilerek istenilen kullanım alanına uygun hale getirilebilmektedir. Nanotellerin karakterizasyonu, nanotellerin nitelikleri ve istenilen kullanım alanının gereksinimleri arasında tekrar üretilebilir bir örtüşme sağlanabilmesi için önem arz etmektedir.

Bu çalışmada (100), (110), (111) düşük indisli yüzeylerden üretilmiş üç farklı kalınlıktaki bakır, gümüş ve altın nanotellerin tek eksen boyunca uygulanan gerinim altındaki yapısal özellikleri incelenmiştir. Klasik moleküler dinamik benzetişimleri 1 K ve 300 K sıcaklıklarında, atomlar arası iki parça etkileşimlerinden oluşan atomistik bir potansiyel kullanılarak gerçekleştirilmiştir. Gerinim nanotellere tek eksen ve tel boyunca uygulanmıştır. Gerinimin kesit geometrisine ve sıcaklığa bağımlılık gösterdiği bulunmuştur. (100) ve (110) yüzeylerinden üretilen nanotellerin (111) yüzeyinden üretilen nanotellere göre gerinim altında daha dayanıklı olduğu bulunmuştur. Sıcaklığın esnekliğe olumlu bir etkisi vardır. Nanoteller parçalanmadan tek boyutlu formlar alamamıştır.

Anahtar Kelimeler: Moleküler Dinamik Benzetişimleri, Bakır Nanoteller, Gümüş Nanoteller, Altın Nanoteller, Gerinim

## **ACKNOWLEDGMENTS**

I would like to express my gratitude to my supervisor Prof. Dr. Şakir ERKOÇ for his guidance, advice, criticism, encouragements, and insight throughout the research.

I would also like to express my gratitude and love to my wife Tuba YAĞLI for her great help and support throughout all the work.

I also want to give my thanks to Sadık KIRATLI and Mustafa ESER for their technical support in the execution of the simulations.

This study was supported by the Turkish Land Forces.

# TABLE OF CONTENTS

ABSTRACT .....	v
ÖZ.....	vi
ACKNOWLEDGMENTS.....	vii
TABLE OF CONTENTS .....	viii
LIST OF TABLES .....	xii
LIST OF FIGURES.....	xiii
CHAPTERS .....	1
1. INTRODUCTION.....	1
1.1. 0D Nanostructured Materials.....	2
1.2. 2D Nanostructured Materials.....	3
1.3. 1D Nanostructured Materials.....	3
1.4. Previous studies in literature.....	8
2. METHOD OF CALCULATION .....	11
2.1. Atomistic Simulation Techniques.....	11
2.1.1. Static Method .....	13
2.1.2. Lattice-Dynamics Method.....	13

2.1.3. Monte-Carlo Method .....	13
2.1.4. Molecular Dynamics.....	14
2.2. Potential Energy Functions Used In Molecular Dynamics .....	19
2.2.1. Erkoç Empirical Model Potential .....	20
2.3. Models Studied and Strain Process .....	22
2.4. Programming artwork .....	24
2.4.1. Parallelization .....	26
3. RESULTS AND DISCUSSION.....	31
3.1. Cu(100) Nanowires .....	31
3.1.1. Cu-100A at 1 K and 300 K.....	32
3.1.2. Cu-100B at 1 K and 300 K.....	33
3.1.3. Cu-100C at 1 K and 300 K.....	34
3.2. Cu(110) Nanowires .....	35
3.2.1. Cu-110A at 1 K and 300 K.....	35
3.2.2. Cu-110B at 1 K and 300 K.....	35
3.2.3. Cu-110C at 1 K and 300 K.....	36
3.3. Cu(111) Nanowires .....	37
3.3.1. Cu-111A at 1 K and 300 K.....	37
3.3.2. Cu-111B at 1 K and 300 K.....	37
3.3.3. Cu-111C at 1 K and 300 K.....	38

3.4. Ag(100) Nanowires .....	39
3.4.1. Ag-100A at 1 K and 300 K .....	39
3.4.2. Ag-100B at 1 K and 300 K.....	39
3.4.3. Ag-100C at 1 K and 300 K.....	40
3.5. Ag(110) Nanowires .....	40
3.5.1. Ag-110A at 1 K and 300 K .....	40
3.5.2. Ag-110B at 1 K and 300 K.....	41
3.5.3. Ag-110C at 1 K and 300 K.....	41
3.6. Ag(111) Nanowires .....	42
3.6.1. Ag-111A at 1 K and 300 K .....	42
3.6.2. Ag-111B at 1 K and 300 K.....	43
3.6.3. Ag-111C at 1 K and 300 K.....	43
3.7. Au(100) Nanowires .....	44
3.7.1. Au-100A at 1 K and 300 K .....	44
3.7.2. Au-100B at 1 K and 300 K.....	45
3.7.3. Au-100C at 1 K and 300 K.....	45
3.8. Au(110) Nanowires .....	46
3.8.1. Au-110A at 1 K and 300 K .....	46
3.8.2. Au-110B at 1 K and 300 K.....	46
3.8.3. Au-110C at 1 K and 300 K.....	47

3.9. Au(111) Nanowires.....	47
3.9.1. Au-111A at 1 K and 300 K.....	47
3.9.2. Au-111B at 1 K and 300 K.....	48
3.9.3. Au-111C at 1 K and 300 K.....	49
3.10. Energy graphics.....	49
4. CONCLUSIONS .....	55
REFERENCES .....	59
APPENDICES .....	67
A. UNIT CELLS TO GENERATE NANOROD MODELS.....	67
B. C++ CUDA KERNEL CODE OF FORCE FUNCTION .....	71
C. FORTRAN CODE OF PARALLEL FORCE FUNCTION .....	73
D. SAMPLE INPUT AND OUTPUT FILES.....	75
E. SIMULATION IMAGES OF COMPLETE STRAIN STEPS FOR CU-111A 300 K .....	79

# LIST OF TABLES

## TABLES

Table 1: Parameters used to determine time step $\Delta t$ . Numerical values are taken from [52].	18
Table 2: Parameters used for the materials studied [55]. In these parameters, energy is in eV and distance is in Å.	22
Table 3: Geometrical parameters of the ideal structures generated.	24

# LIST OF FIGURES

## FIGURES

Figure 1: Schematic representation of periodic boundary condition [54].	19
Figure 2: Initial models common for all materials: a) 100-A b) 100-B c) 100-C d) 110-A e) 110-B f) 110-C g) 111-A h) 111-B i) 111-C	23
Figure 3: Simple flow diagram of the algorithm.	26
Figure 4: OpenMP execution flow diagram.	27
Figure 5: CPU and GPU architectures.	28
Figure 6: CPU vs GPU performance test results.	29
Figure 7: Total potential energy vs MD steps for Cu-100A at 1 K strain step 10.	32
Figure 8: Cu-100A at 1 K and 300 K	33
Figure 9: Cu-100B at 1 K and 300 K	33
Figure 10: Total potential energy vs MD steps for Cu-100C at 300 K	34
Figure 11: Cu-100C at 1 K and 300 K	34
Figure 12: Cu-110A at 1 K and 300 K	35
Figure 13: Cu-110B at 1 K and 300 K	36
Figure 14: Cu-110C at 1 K and 300 K	36

Figure 15: Cu-111A at 1 K and 300 K.....	37
Figure 16: Cu 111B at 1 K and 300 K.....	38
Figure 17: Cu 111C at 1 K and 300 K.....	38
Figure 18: Ag 100A at 1 K and 300 K.....	39
Figure 19: Ag 100B at 1 K and 300 K.....	40
Figure 20: Ag 100C at 1 K and 300 K.....	40
Figure 21: Ag 110A at 1 K and 300 K.....	41
Figure 22: Ag 110B at 1 K and 300 K.....	41
Figure 23: Ag 110C at 1 K and 300 K.....	42
Figure 24: Ag 111A at 1 K and 300 K.....	43
Figure 25: Ag 111B at 1 K and 300 K.....	43
Figure 26: Ag 111C at 1 K and 300 K.....	44
Figure 27: Au 100A at 1 K and 300 K.....	44
Figure 28: Au 100B at 1 K and 300 K.....	45
Figure 29: Au 100C at 1 K and 300 K.....	45
Figure 30: Au 110A at 1 K and 300 K.....	46
Figure 31: Au 110B at 1 K and 300 K.....	47
Figure 32: Au 110C at 1 K and 300 K.....	47
Figure 33: Au 111A at 1 K and 300 K.....	48
Figure 34: Au 111B at 1 K and 300 K.....	48

Figure 35: Au 111C at 1 K and 300 K.....	49
Figure 36: Strain energy with respect to elongation for different sizes of Cu nanowires at 1 K. ....	50
Figure 37: Strain energy with respect to elongation for different sizes of Cu nanowires at 300 K. ....	51
Figure 38: Strain energy with respect to elongation for different sizes of Ag nanowires at 1 K. ....	52
Figure 39: Strain energy with respect to elongation for different sizes of Ag nanowires at 300 K. ....	52
Figure 40: Strain energy with respect to elongation for different sizes of Au nanowires at 1 K. ....	53
Figure 41: Strain energy with respect to elongation for different sizes of Au nanowires at 300 K. ....	53
Figure 42: Unit cell to generate face centered (100) surface.....	67
Figure 43: Unit cell to generate face centered (110) surface.....	68
Figure 44: Unit cell to generate face centered (111) surface.....	68
Figure 45: Initial structure of the nanowire. ....	79
Figure 46: Relaxed structure of the nanowire. ....	79
Figure 47: Relaxed structure of the nanowire after strain step 1.....	80
Figure 48: Relaxed structure of the nanowire after strain step 2.....	80
Figure 49: Relaxed structure of the nanowire after strain step 3.....	80
Figure 50: Relaxed structure of the nanowire after strain step 4.....	81

Figure 51: Relaxed structure of the nanowire after strain step 5. ....	81
Figure 52: Relaxed structure of the nanowire after strain step 6. ....	81
Figure 53: Relaxed structure of the nanowire after strain step 7. ....	82
Figure 54: Relaxed structure of the nanowire after strain step 8. ....	82
Figure 55: Relaxed structure of the nanowire after strain step 9. ....	82
Figure 56: Relaxed structure of the nanowire after strain step 10. The nanowire has fragmented and clustered. ....	83

# CHAPTER 1

## INTRODUCTION

One of the basic concepts of physics and chemistry is that most properties of materials depend on the arrangement of their atoms, i.e. their microstructure. A most striking example of this concept would be the human body. If we separate the human body into its most fundamental building blocks, we would obtain hydrogen, oxygen, nitrogen, and small fractions of carbon and calcium and some other elements [1]. The price of these materials would be very low. But when these elements are properly arranged, we obtain the human body which is priceless in its abundance of abilities like eating, talking, thinking, self-repairing, etc.

The production of materials with specific new properties different from their bulk counterparts, by controlling their microstructure on the atomic level, has become an emerging interdisciplinary field. The use of these materials is expected to have enormous effects on the design and engineering of everything from common consumer products and buildings to sophisticated systems supporting numerous applications in the automotive, aerospace, and other industries [2].

Nanotechnology deals with developing materials, devices, or other structures possessing at least one dimension sized from 1 to 100 nanometers (nanomaterials).

The first classification scheme of nanostructured materials was proposed by Gleiter in 1995 [3]. In this initial work, he proposed three categories of nanostructured materials according to their shape of crystallites; layer shaped, rod shaped, and equiaxed crystallites. Then he separated each of these three categories four groups according to

their chemical composition: the same composition, different composition for different crystallites, different compositions for boundaries and crystallites, crystallites dispersed in matrix of different compositions. The difference of these groups are emphasized with the difference of their size effects and the changes in the atomic structures due to the high density of interfaces. In a later work, Gleiter focuses on the synthesis and properties of the nanomaterials of these groups and tries to summarize the basic physical concepts and the microstructural features of equilibrium and non-equilibrium nanostructured materials [4].

These works did not cover some of the 0D, 1D, 2D, and 3D nanostructures such as fullerenes, nanotubes and nanoflowers. Therefore a later work was done by Skorokhod with a modified classification scheme to group the nanostructures as we mainly do today [5]. A restricted set of nanostructure classes was suggested to build from the constituting elementary units, namely, 0D clusters and particles, 1D nanotubes and nanowires, 2D nanoplates and layers. The 3D units are excluded because they cannot be used to build low dimensional nanostructured materials except 3D matrix. However 3D structures can be considered as nanostructures if they involve the 0D, 1D, and 2D nanostructured materials.

In the following subsections, these classified materials will be introduced in detail. Since 1D nanostructures are the main subject of this thesis, they will be explained after 0D and 2D nanostructured materials.

### **1.1. 0D Nanostructured Materials**

In 0D nanostructured materials (NSMs), which are also called quantum dots or nanoparticles, the quantum confinement effect occurs in all three dimensions [6]. Quantum confinement is the change of electronic and optical properties when the material is of sufficiently small size—typically 10 nanometers or less. The bandgap increases as the size of the nanostructure decreases. Specifically, the phenomenon results from electrons and holes being squeezed into a dimension that approaches the Bohr radius. Because of the resulting density of electronic states, nanowires are expected to exhibit very different optical, electrical, and magnetic properties from their bulk 3D crystalline forms. Some of the differences from the bulk properties are:

increased surface area, very high density of electronic states and joint density of states near the energies of their van Hove singularities, enhanced exciton binding energy, diameter-dependent bandgap, and increased surface scattering for electrons and phonons [7]. With their striking property of configurable optical and electrical properties as function of size [8], 0D nanostructured materials are extensively studied for applications in nanocrystal-based light-emitting diodes [9], quantum-dot-sensitized solar cells with improved efficiency [10], modulation-doped field effect transistors [11], and long-wavelength quantum dot lasers [12].

## **1.2. 2D Nanostructured Materials**

2D nanostructures have two dimension larger than the nanoscale. Nanomaterials such as nanosheets, nanofilms, nanodisks, nanowalls, nanoprisms, and nanoplates fall into this category. Due to the high reactivity and oxidative stress it introduces, carbon nanotube-based nanofilms can act as permanent antimicrobial surfaces, offering the possibility of infection-resistant biomedical and other health care-related devices. Also films of independently controllable bioactivity and mechanical rigidity are achieved by either surface cross-linking or nanoparticle templating approaches and offer great promise to interface the material and biological worlds [13]. Another use of 2D nanostructures is the production of graphene films to be used in numerous applications including large-scale flexible, stretchable, and foldable transparent electronics due to its outstanding optical, electrical, and mechanical properties [14, 15]. New 2D nanostructured nanomaterials provide an alternative route to stretchable electronics. The most successful approaches use elastic conductors as electrical interconnects between active devices that are rigid or only bendable [16]. The commercial success of ultra-thin cellphones and laptop computers with hinged displays, sliding keyboards, and related components motivates the development of sophisticated multilayer flexible interconnection cables and printed circuit boards that can accommodate being bended into small radii of curvature.

## **1.3. 1D Nanostructured Materials**

In the last decade, 1D NSMs have attracted a growing interest due to their wide range potential applications and their importance in research and developments. It is generally accepted that 1D NSMs are ideal systems for exploring a large number of

novel phenomena at the nanoscale and investigating the size and dimensionality dependence of functional properties. They are also expected to play an important role as both interconnects and the key units in fabricating electronic, optoelectronic, and electro chemical energy devices with nanoscale dimensions [17].

Important advances in the research and development of nanowires and nanorods took place after advances in microscopy and characterization techniques reached smaller length scales down to individual atoms.

Nanowires exhibit some properties that are very different from their bulk counterparts. What makes the nanowires interesting is that material properties that are not changeable in bulk materials can be controlled to fit the requirements of the intended application area [18]. The number of conducting channels increases linearly with nanowire diameter. This can be attributed to the increase of available conducting states as the number of atoms in the nanowire increases.

The ability to achieve controllable functional electronics on truly macroscales using printed nanowire arrays presents a feasible route towards their implementation for practical applications. It has been shown that using nanowires, highly flexible and mechanically bendable electronics and sensors can be produced to develop an artificial skin that can give the sense of touch [19].

Characterization of nanowires is important in order to establish a reproducible relationship with the characteristics of nanowires and the desired functionality. Because of the high surface-to-volume ratio in nanowires, their properties depend very much on the surface conditions and geometry. Nanowires of the same material can show different mechanical properties depending on their aspect ratios, surface conditions and Miller indices. The Young modulus of ZnO nanowires with diameters smaller than 120 nm increases dramatically with decreasing diameters, and is significantly higher than that of the larger ones whose modulus tends to that of bulk ZnO [20].

The small sizes and high surface-to-volume ratios of 1D nanostructures endow them with a variety of interesting and useful mechanical properties. Their high stiffness and

strength make them suitable for applications in tough composites and as nanoscale actuators, force sensors, and calorimeters. A piezoelectric field effect transistor has been applied as a force/pressure sensor for measuring forces in the nanonewton range and even smaller with the use of smaller nanowires. An almost linear relationship between the bending force and the conductance was found at small bending regions, demonstrating the principle of nanowire-based nanoforce and nanopressure sensors [21]. One-dimensional nanostructures also showcase unique stability effects driven by the dominance of their surfaces and internal interfaces. As the scale of materials reduces to nanometers, the tendency of surfaces to minimize their free energy may drive structural changes that propagate into the bulk. A rubber-like pseudoelastic behavior is discovered in single-crystalline face-centered-cubic (FCC) Cu nanowires in atomistic simulations. Nonexistent in bulk Cu, this phenomenon is associated primarily with a reversible crystallographic lattice reorientation driven by the high surface-stress-induced internal stresses due to high surface-to-volume ratios at the nanoscale level. The temperature-dependence of this behavior leads to a shape memory effect [22]. Nanowire synthesis techniques can yield single-crystalline structures with a much lower density of line defects than is typically found in bulk materials. As a result, 1D nanostructures often feature a mechanical strength, stiffness, and toughness approaching the theoretical limits of perfect crystals, making them attractive for use in composites and as actuators in nanoelectromechanical systems (NEMS). By self-assembling nanoparticles of platinum on single-wall carbon nanotube templates, hybrid nanowires of platinum were fabricated with extremely high surface area-to-volume ratio. These nanowires showed reversible strains by modulating the surface electronic charge density through an applied potential relative to an electrolyte. These results show the applicability of hybrid metallic nanowire systems for artificial muscle applications [23].

While silicon is the most popular material in nanowire synthesis: gold, copper, and silver are also largely researched as nanowire materials. The materials selected vary according to intended application area.

For example, many studies have focused on the fabrication of copper nanowires because of their potential applications in the micro/nanoelectronics industry and, in

particular, for interconnection in electronic circuits. Copper is one of the most important metals in modern electronic technology. The key characteristic of experiments measuring the conductance of a nanowire while it is being elongated is that there are sudden jumps in conductance, which correlate with discontinuities in the force [24].

Gold nanowires that are 30 nm axially and up to 20 microns in length are finding use as an alternative or complimentary material to carbon nanotubes. They are highly conductive, more transparent, and unlike silver nanowires, are resistant to corrosion or oxidation. Nanowires have shown to be useful as a carbon nanotube replacement in touchscreen displays and transparent electrodes. Nanostructured materials also offer the possibility of 3D device geometries in addition to more conventional planar geometries and allow for precise optimization of critical device dimensions and length scales. It is shown in a recent work that the incorporation of a highly conductive 1D material, such as gold nanowires, can increase carrier extraction from 0D nanocrystalline CdSe [25]. It is also demonstrated in the same work that the photoresponse of the CdSe/gold hybrid material can be controlled by changing the conductivity of the Au nanowires. Through the formation of a hybrid material, they were able to circumvent the low electrical conductivity of nanocrystalline material and demonstrate the potential for a future solid-state nanocrystalline solar cell with improved carrier extraction [25]. Among all, gold nanorods are found to be more popular and useful for potential applications such as biochemical sensing, biomedical diagnostics, and therapeutics due to possible tuning of their surface plasmon resonance in the visible and near-infrared region, which is the potential window of the electromagnetic spectrum for in vivo applications. Thus gold nanowires show promise when used as highly sensitive electronic biosensors. Surface coating of nanorods with poly styrene sulfonate significantly increased the cell viability and showed easy intracellular uptake of the nanorods, which suggests their possible use for different biomedical applications. This rapid, sensitive, and label-free approach for detection of molecular binding events using surface-modified gold nanorods may provide a novel optical multiplex biosensor platform and may have broad potential applications in immunoassay and disease diagnosis [26].

Gold nanorods have been researched for their cytotoxicity effects on cancer cells, laser heating of intracellular gold nanorods to produce thermal damage to malignant cells. They have also been researched for effects of combining external therapeutic photon beam with gold nanorods on cancer cells to establish whether gold nanorods are efficient mediators of converting laser energy into an effective tumor killing agents via thermal cell necrosis. The combination of the laser light and gold nanorods produced very efficient localized cell death effect. Thus their usage in photothermal cancer therapies and in enhancing in-vivo imaging using photoacoustics and highly efficient non-linear optics such as four wave mixing show great promise [27].

Silver nanowires have a lot of optical usages and surface functionalized silver nanorods allow for the particles to be preferentially adsorbed at the surface using chemically bound polymers. Recently, pioneering methods have been developed using silver nanowire networks to achieve transparent conductors, which show comparable performance to commercial indium tin oxide which is currently the most popular transparent conductive film [28].

Nanotechnology has various potential military applications, especially in the field of sensors, transducers, nanorobotics, nanoelectronics, propellants, and explosives to enhance the performance of weapon systems and devices. Nanotechnology is going to play a very important role in the development of materials and devices that will have major roles in military applications as well as societal changes. An example is the usage of nanowires capable of conducting electricity in various new forms of memories and storage devices. A new paradigm appears where magnetization dynamics and charge currents act on each other in nanostructured artificial materials. Due to this phenomena in nanowires, spin currents could even replace charge currents for the transfer and treatment of information, allowing faster, low-energy operations and spin electronics can replace current electronics [29]. Militaries of many countries are aiming towards weapons based on nanotechnology. The human body has developed a tolerance to most naturally occurring elements and molecules with which it has contact. However, it has no natural immunity to new nanosubstances and therefore is more likely to find them toxic. Besides toxic weapons, nanomaterials can be used to develop nanorobots, sensors, transducers, and smart uniforms for soldiers.

The reduction in size of the systems from computers to wireless phones is a continuing trend for electronic defense systems [30]. Another example of military application would be the use of nanowire chemical sensors in biological and chemical warfare threat detection. Nanowires are prepared by the electrodeposition of metal at step edges present on a graphite surface. These nanowires can be used to connect metal nanoparticles (Ni, Au, etc.). Once transferred in a polymer cast, they can operate as sensors. Step edge decoration by electrodeposition on graphite surfaces allows the organization of metal particles and wires at the nanometric scale. By transferring these particles and wires into a polymer cast and contacting these nanocircuits, a palladium nanowire-based sensor for hydrogen gas has been developed. By choosing the nature of the metallic compound for the nanowires and for the nanoparticles, specific nanosensors can be conceived for a large variety of gases as well as for various species and biomolecules in solution [31].

A technique for fabrication of metal nanowires with controlled widths was presented by Natelson et.al. allowing the production of nanowires from a variety of materials on a size scale below 10 nm. The smallest wire diameters achieved through this technique lead to relatively large quantum corrections to the wire conductance even at relatively high temperatures [32]. This technique and its variants can be used to produce samples for studying systems on length scales which fall in the range of length which are the focus of this thesis.

#### **1.4. Previous studies in literature**

Previous simulation studies on this area focus on molecular dynamics (MD) simulations on Cu and Au nanowires. Mechanical responses of FCC nanowires dependent on size and strain have been investigated and revealed that momentum induced disorder plays an important role in the phase transformations during the deformation. The simulation scale is set to 24000 atoms to study a large metallic nanowire with a 6 nm characteristic size scale. Au nanowire is studied in conjunction with Pt nanowire. The effects that size and strain rate have on the stretching behavior of these nanowires are investigated through the simulation of nanowires with three characteristic sizes of 2, 4 and 6 nm, subjected to three distinct strain rates. The selected strain rates produce three distinct modes of deformation, namely crystalline-

ordered deformation, mixed-mode deformation and amorphous-disordered deformation, respectively. A Doppler red-shift effect is observed when the nanowires are strained at the highest strain rate of  $4.0 \times 10^{10} \text{s}^{-1}$ . This effect is most pronounced for the nanowire subjected to the largest stretch velocity. As a result, a constrained dynamic free-vibration phenomenon is observed during stretching, which eventually leads to delocalized multiple necking, instead of a single localized neck when it is strained at a lower rate [33]. Another study on the stress-strain relationship of thin nanowires have applied MD simulation and showed that high temperatures exhibit more complex stress-strain phenomena. In the simulation, the multi-shell helical structures are constructed and originated from Au (111) planes, being rolled up with a certain helical angle. The many-body tight-binding potential is employed to simulate the interatomic force between the gold atoms. The yielding stress of the nanostructure is much higher than that of the FCC structure at 1 K, which can be explained as a result of the smallness of the nanowire. The ultrathin multi-shell nanowire with a diameter of 0.6 nm is stronger than the FCC structure with a diameter of 3 nm. At high temperature, stretched nanowires twist and exhibit more complicated stress-strain phenomena and finally form a cluster of three atoms in cross-section before it breaks [34]. Dunn et al. have performed atomistic simulations on square cross-section FCC gold nanowires aligned in the  $\langle 100 \rangle$  and  $\langle 111 \rangle$  directions and found an increase in Young modulus with a decrease of cross-sectional area. In the paper, the effects of the surfaces and edges on the structure and elastic properties of gold (Au) nanowires is studied. The atomistic simulations are performed using the modified embedded atom potential. In the conclusion of their work, they state that the tensile surface stresses on the sides of the wire cause the wire to contract along the length with respect to the original FCC lattice, and they characterize this deformation in terms of an equilibrium strain versus the cross-sectional area. They also use two methods to compute the effective axial Young moduli, one based on a definition in terms of the strain derivative of the total energy and another in terms of the virial stress often used in atomistic simulations. Both gives quantitatively similar results, showing an increase in Young modulus with a decrease of cross-sectional area in the  $\langle 111 \rangle$  and  $\langle 100 \rangle$  wires that do not undergo a phase transformation [35]. In another study, mechanical deformations of Cu (100) nanowires have been investigated in cases of elongation, shearing, rotation, rotated elongation, and different yielding and fracturing

mechanisms have been shown. The steepest-descent method has been used for the simulations. The investigated subjects are yielding, rearrangement, structural transition, and mechanisms of fracture of Cu nanowires by an external agent. The potential function used is the second-moment approximation of the tight-binding scheme. Before the first yielding, nanowires preserved the elastic stages, and after this the mechanical deformation proceeded in alternating quasi-elastic and yielding stages. The first yield strain in the case of rotated elongation was one-half of that in the elongation case, and shear forces in the case of rotated elongation appeared at  $16^\circ$  after the first yield [36]. Wu applied an embedded-atom model to study mechanical properties of copper nanowires using MD simulations and obtained results showing the importance of surface atoms in mechanical behavior of nanostructures. Three-dimensional molecular dynamics simulations of the mechanical properties of rectangular cross-section copper nanowire are executed. A stable free-relaxation state and the stress–strain relation of nanowire under extension are obtained. The elastic modulus, yielding strength and deformation are studied. The surface effect, size effect, and temperature effect on the extension property of metal nanowire are discussed in this work [37].

In the present study, mechanical properties of three different materials, copper, silver and gold nanowires are investigated. A uniaxial strain has been applied to all three materials in atomistic simulations. Classical molecular dynamics simulations have been conducted on the nanowires generated from three low-index surfaces (100), (110) and (111) for all the three materials. For the simulations, cylindrical models have been prepared to resemble reproducible nanowires. Three different widths for each surface of each material have been prepared, resulting in 9 different models for each material. The simulations have been performed at two different temperatures: 1 K and 300 K. A 5% strain per one step have been applied to the models and the stability of the materials has been investigated. Results have been obtained for 54 different simulations in total.

## CHAPTER 2

### METHOD OF CALCULATION

Computer simulation techniques are used to calculate the structures and properties of molecules and solids such as interaction energies, electronic charge distributions, dipoles and higher multipole moments, vibrational frequencies, reactivity or other spectroscopic quantities, and cross sections for collision with other particles.

#### 2.1. Atomistic Simulation Techniques

Highly accurate methods called *ab initio* methods are based entirely on quantum mechanics and use solutions of the molecular Schrödinger equation. These methods do not include any empirical or semi-empirical parameters in their equations and are derived directly from theoretical principles, with no inclusion of experimental data. But as the system size grows in this method, the computational resources required grows exponentially. Thus, most *ab initio* calculations make the Born–Oppenheimer approximation, which greatly simplifies the underlying Schrödinger equation by assuming that the nuclei remain in place during the calculation [38]. Despite these approximations *ab initio* methods remain a very computationally expensive method.

Semi-empirical methods are based on the Hartree–Fock formalism which is a method of approximation for the determination of the wave function and the energy of a quantum many-body system in a stationary state [39]. The method makes many approximations and obtain some parameters from empirical data and is very important in atomistic simulations where the full Hartree–Fock method without the approximations is too expensive. Semi-empirical calculations are much faster than

their ab initio counterparts since some pieces of information are parameterized in such a way as to produce results that best agree with experimental data.

Density functional theory (DFT) is a computational quantum mechanical modelling method used to investigate the electronic structure of many-body systems, in particular atoms, molecules, and the condensed phases. DFT determines the properties of a many-electron system by using functionals, i.e., functions of another function, which in this case is the spatially dependent electron density which reduces the computational cost greatly. But the computational requirements are still very high for large systems. There are also difficulties in using density functional theory to properly describe intermolecular interactions, especially van der Waals forces (dispersion); charge transfer excitations, transition states, global potential energy surfaces, dopant interactions, and some other strongly correlated systems, and in calculations of the band gap and ferromagnetism in semiconductors [40].

Atomistic computer simulation (ACS) techniques calculate the properties of a collection of atoms which interact with one another through a potential energy function (PEF). Such a PEF, in principle, describes the behavior of the ground state electronic energy as a function of the nuclear coordinates, so that all of the basic quantum physics is implicitly captured in the functional behavior of the PEF. In practice, the PEF cannot yet be determined in any consistent fashion from quantum mechanical methods, so semi-empirical (or totally empirical) models must be utilized [41].

There are four basic ACS methods in use: Statics, Monte-Carlo, Molecular-Dynamics, and Lattice-Dynamics [41]. The common thread of all these methods is their application to the determination of macroscopic properties from a microscopic description of the Born-Oppenheimer potential using numerical methods on high-speed computers [42].

### 2.1.1. Static Method

The static method is the most simple of these methods. An initial configuration of the system is given as input and the force on any atom is calculated using the PEF as in the equation

$$F_i = -\nabla_i\Phi \quad (1)$$

Then all of the atoms are displaced according to the net force applied to each of them. The static method finds the relaxed configuration of atoms using conjugate gradient or some similar (constrained) minimization of the total energy. This provides information about crystal lattice structure in different phases and under different conditions. It has been shown that the static method is quite insensitive to the instability of atomic structure especially without thermal fluctuation and might not be a suitable tool for studying the behavior of nanomaterials beyond the elastic limit [43].

### 2.1.2. Lattice-Dynamics Method

The theory of lattice dynamics relies on the ability to expand the crystal energy in terms of small atomic displacements to quadratic order [44]. The dynamical matrix lends itself naturally to simulations using empirical calculations, where the second derivatives are easily computed. The values of the force constants are calculated from the empirical energy functions. The analytic representation of the atomic motion is generated by considering only small amplitude, low temperature vibrations of the atoms about some stable point of the PEF surface where the curvature of the surface at that point suffices to characterize the atomic motion [41].

One important application of lattice dynamics models is the computation of thermodynamic properties [45].

### 2.1.3. Monte-Carlo Method

The Monte-Carlo method relies on repeated random sampling of atomic configurations to obtain an approximate of the canonical ensemble of the system of atoms. The constraints of constant volume and number of atoms are automatically satisfied by the use of periodic boundary conditions [41]. A short explanation of the

algorithm is as follows. Small random displacements are applied to an atom and the resulting change in energy,  $\Delta\Phi$ , is calculated using the PEF. If  $\Delta\Phi$  is negative, the displacement of the atom is accepted as the new configuration. If  $\Delta\Phi$  is positive, the Boltzman factor  $e^{-\Delta\Phi/kT}$  is calculated with a desired temperature T and is compared to a random number to select a new random configuration.

#### 2.1.4. Molecular Dynamics

Molecular dynamics (MD) is the determination of physical movements of atoms and molecules in a computer simulation using N-body simulations [46]. In this method, we start with a configuration of atoms, and use either empirical or quantum mechanical methods to compute the force on each atom by numerically integrating Newton's equation of motion (2) for a collection of N atoms interacting through a specific analytic PEF and subject to periodic boundary conditions that constrain the volume and number of atoms. With information on the current and previous atomic positions, this force is converted to acceleration, and using a numerical time step algorithm, that will be later explained, the next position of each atom can be predicted. When done with sufficient accuracy, the total energy in the system will be constant, thus the molecular-dynamics method generates a time-ordered series of atomic configurations which, taken as a whole, approximate the microcanonical ensemble for the system.

$$\frac{\partial^2 x_i}{\partial t^2} = -\frac{1}{m_i} \nabla_i \Phi \quad , \quad i = 1, 2, \dots, 3N \quad (2)$$

Modification of the technique can allow constant pressure or temperature ensembles to be generated. In this thesis, the experiments are conducted with constant temperature. To achieve the constant temperature, simple velocity scaling thermostat method is used in the simulations [41]. The main problem in the method is to find the forces applied to each atoms at any time according to the interactions between the atoms. The selection of an appropriate interatomic potential with enough complexity and flexibility is crucial to accurately portray real matter in a sufficient efficiency.

All choices include approximations based on Born-Oppenheimer approximation. When the absence of external forces is assumed, the total energy of  $N$  interaction particles can be expressed as

$$E_N = \phi_1 + \phi_2 + \phi_3 + \dots + \phi_n + \dots \quad (3)$$

where  $\phi_n$  represents the sum of  $n$ -body interaction energy. If the particles are non-interacting the equation becomes

$$E'_N = \phi_1 \quad (4)$$

The difference between these two energies gives us the interaction energy of  $N$  interacting particles as a function of their position.

$$\Phi = E_N - E'_N = \phi_2 + \phi_3 + \dots + \phi_n + \dots \quad (5)$$

$$\Phi = \Phi(r_1, r_2, \dots, r_N) \quad (6)$$

$$\phi_2 = \sum_{i < j} U_2(r_i, r_j) \quad (7)$$

where  $U_2$  represent two-body interactions. The quantity  $\Phi$  is defined as the total configuration energy of the system and is a measurable quantity. In this many-body expansion, the series has a quick convergence and the higher moments can be neglected so that the complexity of the computations can be reduced and the size of the simulated systems can grow [47]. The contribution of these truncated terms can be included into the empirical potential energy function with the use of various linear or non-linear parameters [48].

#### 2.1.4.1. Verlet Algorithm

The forces acting on the elements of the system is calculated as

$$F_i = -\nabla_i \Phi \quad (8)$$

The velocities are calculated from

$$F_i = m_i \frac{dv_i}{dt} \quad (9)$$

In our molecular dynamics simulations, we will be using Verlet algorithm [49] as the time integration algorithm. Verlet algorithm is the most commonly used time integration algorithm in molecular dynamics. The basic idea behind the algorithm is to write two third-order Taylor expansions for the positions  $r(t)$ , one forward and one backward in time. Calling  $v$  the velocities,  $a$  accelerations, and  $b$  the third derivatives of  $r$  with respect to  $t$ , one has

$$r(t + \Delta t) = r(t) + v(t)\Delta t + \left(\frac{1}{2}\right)a(t)\Delta t^2 + \left(\frac{1}{6}\right)b(t)\Delta t^3 + O(\Delta t^4) \quad (10)$$

$$r(t - \Delta t) = r(t) - v(t)\Delta t + \left(\frac{1}{2}\right)a(t)\Delta t^2 - \left(\frac{1}{6}\right)b(t)\Delta t^3 + O(\Delta t^4) \quad (11)$$

Adding the two expressions gives us the basic form of the Verlet algorithm.

$$r(t + \Delta t) = 2r(t) - r(t - \Delta t) + a(t)\Delta t^2 + O(\Delta t^4) \quad (12)$$

The truncation error of the algorithm when evolving the system by  $\Delta t$  is of the order  $\Delta t^4$ , even third derivatives do not appear explicitly. With this version of the Verlet algorithm the velocities are not directly generated. The velocities are required to compute the kinetic energy whose evaluation is necessary to test the conservation of the total energy of the system,  $E=K+V$ . The velocities can be computed from the positions by using

$$v(t) = \frac{r(t + \Delta t) - r(t - \Delta t)}{2\Delta t} \quad (13)$$

The Equation (13) gives us the velocities of the atoms which then will be used to calculate the kinetic energies of individual atoms.

### 2.1.4.2. Predictor-Corrector Algorithm

Another commonly used class of method to integrate the equations of motion is predictor-corrector algorithms [50]. The most often used versions consist of three steps. The first step is the predictor. From the positions and their time derivatives up to a certain order  $q$ , all known at time  $t$ , one predicts the same quantities at time  $t + \Delta t$  by means of a Taylor expansion. Among these quantities are, of course, accelerations  $\mathbf{a}$ . The second step is the force evaluation. The force is computed taking the gradient of the potential at the predicted positions. The resulting acceleration will be in general different from the predicted acceleration. The difference between the two constitutes an error signal. The third step is the corrector. The error signal in the second step is used to correct positions and their derivatives. All the corrections are proportional to the error signal, the coefficient of proportionality being a magic number determined to maximize the stability of the algorithm.

### 2.1.3.3. Time Step Determination

In the molecular dynamics simulation, the atoms included in molecules move according to the Newtonian equation of motions. In other words, when we know the structure of molecule at one moment, we can find the structure at the next moment using the integration method of the equation of motion with time starting from there. The process of integrating the equation of motion can be achieved by several kinds of algorithm and in this work we use the time step method ( $\Delta t$ ). If a big time step is used, the motion of molecule becomes unstable due to the very big error occurring in the integration. Therefore, molecules may not have a normal structure any more. Reversely, if a very small value of time step is used, it will not be efficient due to a very long calculation time [51].

From the conservation of total energy ( $E = E_k + E_p$ ) and considering a diatom, one can write the equality [41]

$$\frac{1}{2}mv^2 = E \quad (14)$$

where  $m$  is mass,  $v$  is velocity. This equation can be rewritten as

$$\frac{1}{2} m \left( \frac{\Delta r}{\Delta t} \right)^2 = E \quad (15)$$

Here  $\Delta r$  can be taken as the equilibrium distance  $r_0$ , and  $E$  as the equilibrium energy  $\epsilon_0$ . Then  $\Delta t$  becomes

$$\Delta t = \sqrt{\frac{mr_0^2}{2\epsilon_0}} \quad (16)$$

In practice the molecular dynamics time step ( $DT$ ) is usually taken as one hundredth of this value, namely  $DT = \Delta t/100$ .

For the materials in this thesis, the constants that will be used in time step calculation are tabulated in Table 1.

Table 1: Parameters used to determine time step  $\Delta t$ . Numerical values are taken from [52].

	Cu	Ag	Au
$m$	63.546 amu	107.8682 amu	196.9665 amu
$r_0$	2.22 Å	2.48 Å	2.47 Å
$\epsilon_0$	2.01 eV	1.65 eV	2.29 eV

#### 2.1.3.4. Periodic Boundary Conditions

In molecular dynamics simulations, the simulation box size must be large enough to avoid boundary condition artifacts. Boundary conditions are often treated by choosing fixed values at the edges (which may cause artifacts), or by employing periodic boundary conditions in which one side of the simulation loops back to the opposite side, mimicking a bulk phase which allows us to simulate a large system by modelling only a small part. The system is made pseudo-infinite by the application of periodic boundary conditions in the three Cartesian directions. This is achieved by the “nearest image convention” [53]. In computing pair vectors between two particles  $i$  and  $j$  one

needs only differences of coordinate values. If this coordinate difference  $\Delta x_{ij} \equiv x_j - x_i$  is larger than  $L/2$  where  $L$  is the length of the cell, then the particle  $j$  will not be regarded as an interaction partner of  $i$ ; instead, its left periodic image with coordinate  $x_j - L$  interacts with  $i$ .

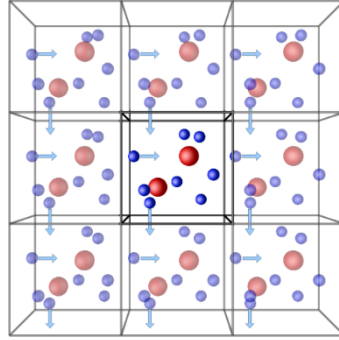


Figure 1: Schematic representation of periodic boundary condition [54].

## 2.2. Potential Energy Functions Used In Molecular Dynamics

Many physical properties of matter may experimentally be observed. While quantum mechanical methods give accurate results, they require a large computational effort and are limited to studies of static properties. Furthermore, quantum mechanical methods are currently applicable for systems involving a small number of atoms. On the other hand, empirical interatomic potentials can handle much larger systems and they can be used to study static as well as dynamic properties. Many of the atomistic computer simulation techniques are based on empirical model potentials describing interactions among the atoms in the system. In atomistic level simulations atoms are considered as point-like particles and no electronic information, nor nuclear information is present. The advantage of computer simulation is that we know exactly what is being measured. The disadvantage is that the results obtained are only as good as the potential energy function used in the simulations. Model potentials are usually empirical; they contain adjustable parameters (linear and/or non-linear). Many-body interactions (in microscopic scale) may be separated as the interactions among the internuclear particles, among the electrons in an atom, molecule or solid, and finally among the atoms within a molecule, solid, liquid, or gas [45].

The properties that can be studied using empirical potential energy functions can be grouped as bulk, surface, cluster, collisions, nanostructures, radiation damage, and electronic [41]. Bulk properties that can be studied fall into subgroups as structural properties (lattice structure, vacancy, defects, interstitials, amorphization, and melting), energetics (cohesive energy, vacancy formation, and defect energies), thermo dynamical properties (heat capacity, heat of formation, and phase diagrams), elastic properties (bulk modulus, elastic constants, and liquid properties), and phonon dispersion frequencies (lattice vibrations). Surface properties that can be studied fall into subgroups as structural properties (surface reconstruction, multilayer relaxation, steps, facets, vacancy, defects, melting, adsorption, chemisorption and physisorption), energetics (surface energy and vacancy formation), thermo dynamical properties (as heat of adsorption), interface structure, thin films (structures), and atomic force microscope. Cluster properties that can be studied fall into subgroups as stability (structure), energetics, dynamics, melting, and some spectroscopic properties (vibrational). Collision simulations allow studies of atom–surface, molecule–surface, cluster–surface, and cluster–cluster collisions. Nanostructures like the topic of this thesis can be studied in subgroups like nanowires, nanomachines, etc. Radiation damage on bulk, surface, and clusters may also be studied. But electronic properties like superconductivity, magnetic, optical, and some spectroscopic studies like transitions cannot be studied by using empirical potential energy functions.

### **2.2.1. Erkoç Empirical Model Potential**

In these atomistic level computer simulations the *Erkoc empirical model potential (I)* was used [55]. In the usual form, in order to make up for the contribution of the truncated terms, the total PEF can take one linear parameter. However when the two-body terms are separated more linear parameters can be inserted into the total PEF. This is done by separating the pair-interaction function into two parts, which usually consists of two terms: a repulsive term and an attractive term.

The *Erkoc potential (I)* is formed from pair interactions, which contains many-body effects and it has been parameterized for the FCC metal elements copper, silver and gold [56].

The total energy of the system is expressed as the linear combination of two two-body functions [56], given as

$$\Phi = \phi_2 = D_{21}\phi_{21} + D_{22}\phi_{22} \quad (17)$$

where  $\phi_{21}$  and  $\phi_{22}$  are two-body energies

$$\phi_{2k} = \sum_{i<j} U_{ij}^{(2k)}, \quad k = 1,2 \quad (18)$$

The general form of the two-body atomic interactions in terms of inter-atomic distances is defined as

$$U_{ij}^{(2k)} = A_k r_{ij}^{-\lambda_k} e^{-\alpha_k r_{ij}^2} \quad (19)$$

The two-body interaction function contains three parameters ( $A_k, \lambda_k, \alpha_k$ ) which will be modified considering the bulk cohesive energy and bulk stability condition. In this form, the pair-potential function does not give a bound state for a dimer. It requires two such function: one for the repulsive branch and one for the attractive branch of complete pair-potential function. A combination of two such functions form an exact pair-potential function:

$$U_{ij} = U_{ij}^{21} + U_{ij}^{22} \quad (20)$$

As a result, there are two sets of parameters for the two-body potential functions: one for the repulsive part ( $A_1, \lambda_1, \alpha_1$ ) in  $U_{ij}^{21}$  and one for the attractive part ( $A_2, \lambda_2, \alpha_2$ ) in  $U_{ij}^{22}$ . These parameters have been determined by fitting the exact pair-potential function (20) to the experimentally determined curve, which are taken from a previous work by Erkoç [57] for the elements considered in this thesis. The exact pair-potential with parameters  $D_{21}$  and  $D_{22}$  represents effective pair potential.

Table 2: Parameters used for the materials studied [55]. In these parameters, energy is in eV and distance is in Å.

<b>Parameters</b>	<b>Cu</b>	<b>Au</b>	<b>Ag</b>
$A_1$	110.766008	345.923364	220.262366
$\lambda_1$	2.09045946	1.0428923	1.72376253
$\alpha_1$	0.394142248	0.750775965	0.673011507
$A_2$	-46.1649783	-38.9245908	-26.0811795
$\lambda_2$	1.49853083	1.05974062	1.81484791
$\alpha_2$	0.207225507	0.229377368	0.120620395
$D_{21}$	0.436092895	0.888911352	1.00610152
$D_{22}$	0.245082238	0.254280292	0.221234242

### 2.3. Models Studied and Strain Process

In atomistic computer simulation applications, particularly in surface science, crystal physics and chemistry, and in many other applications in materials sciences, in general, crystal structure and therefore surface structure are used. One first has to generate a particular surface structure [41]. To achieve this, we must build a unit cell formed according to the related surface and repeat it in the directions needed.

The materials that are studied in this thesis are all face-centered-cubic (FCC) materials and as a result all have the same unit cell structure. The difference of the models that will be created for these materials is their lattice constants so the models will have the same initial shape for all the materials but will be scaled proportional to the lattice constant of the simulated material. The details of the unit cells to generate the nanorod models are given in Appendix A [41].

To start building our model with 3D coordinates, we will take the bottom left of the first unit cell as the coordinate 0, 0, 0 (x, y, z). Then we will repeat the FCC unit cell in x and y directions to obtain the required diameter size of the nanowire model. Then this model will be repeated along the z axis to obtain the required length for the nanowire. Finally, outer atoms at the corners of the obtained rectangular nanowires will be removed to obtain circular cross-section models resembling real nanowires

obtainable from synthesis. Changes to the models were applied to the models to obtain circular cross-sections for these simulations as they presented the most stable and natural cross-sectional configuration [58].

Models were generated for three low dimensional, namely (100), (110), and (111) surfaces. As the working material of this thesis, three different size for each surface have been generated. The results were 3 different sized models for each surface and 9 different shaped models in total. These models are shown in Figure 2. The visualization of the models were done using Jmol, an open-source Java viewer for chemical structures in 3D [59].

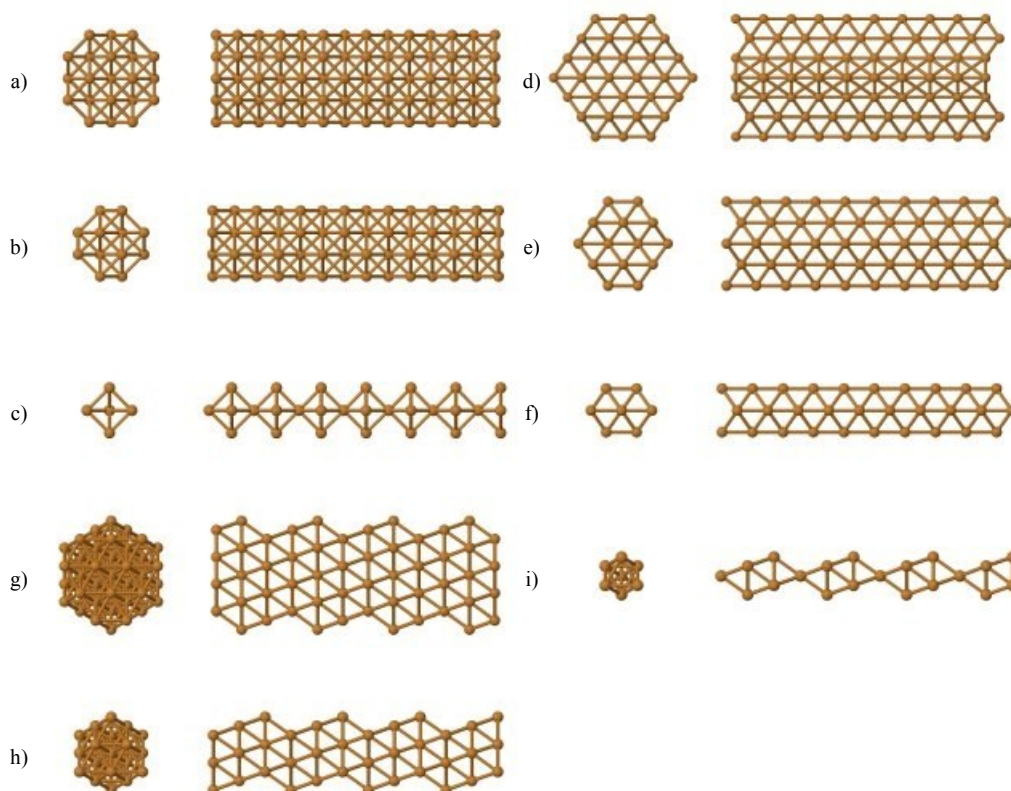


Figure 2: Initial models common for all materials: a) 100-A b) 100-B c) 100-C  
d) 110-A e) 110-B f) 110-C g) 111-A h) 111-B i) 111-C

Since the lattice positions of these 9 different models are similar for each of the three FCC materials studied, the only difference was the proportions of the models changing

relative to their lattice constants. By scaling the 9 initial models create for copper according to the ratio of the lattice constant, we obtained 27 different models. Geometrical parameters of all the models are given in Table 3.

All of the prepared models were input into the simulations under 1 K and 300 K to observe the effect of the temperature on the mechanical properties of the nanowires. So the results in the thesis will include data from 54 different MD simulations.

Table 3: Geometrical parameters of the ideal structures generated.

Models	Radius (Å)			Length (Å)			# of atoms		
	Cu	Ag	Au	Cu	Ag	Au	Cu	Ag	Au
100-A	8.07	9.15	9.14	23.53	26.59	26.52	147		
100-B	5.71	6.47	6.45				84		
100-C	3.61	4.09	4.08				35		
110-A	12.75	14.46	14.41	24.23	27.47	27.41	300		
110-B	7.66	8.68	8.66				140		
110-C	5.1	5.78	5.76				70		
111-A	8.84	10.02	9.99	22.91	25.97	25.91	148		
111-B	5.89	6.67	6.65				76		
111-C	2.96	3.35	3.34				28		

## 2.4. Programming artwork

The algorithm of the working program is as follows:

1. Read the PEF parameters, time step, and atomic mass parameters.
2. Read the input data:
  - a. The title of the simulated model.
  - b. Number of molecular dynamic steps to be executed.
  - c. Periodic boundary conditions.
  - d. Temperature.
  - e. Number of atoms and their coordinates.
3. Sort the atoms by the z axis and find the boundary limits of the model.
4. Calculate the initial potential energy of each atom and the initial force that each atom experiences.
5. Set initial velocities according to Maxwell velocity distribution.

6. Print the initial status of the system (initial velocities, potential energies, forces, total energy, and temperature).
7. Start MD steps.
8. Reposition any particle outside the periodic boundary region.
9. Calculate the forces acting on each atom.
10. Compute the positions at time step  $n+1$ .
11. Calculate the forces acting on each atom.
12. Compute the velocities at time step  $n+1$ .
13. Calculate the temperature that system reached by calculating the kinetic energy of each atom.
14. Calculate the scaling factor and scale the velocities.
15. Calculate total energy of the system.
16. Print the coordinates and the energies of the system according to the periodic printing parameter.
17. Go to step 8 if the number of MD steps is not completed.
18. Print the final state of the system.

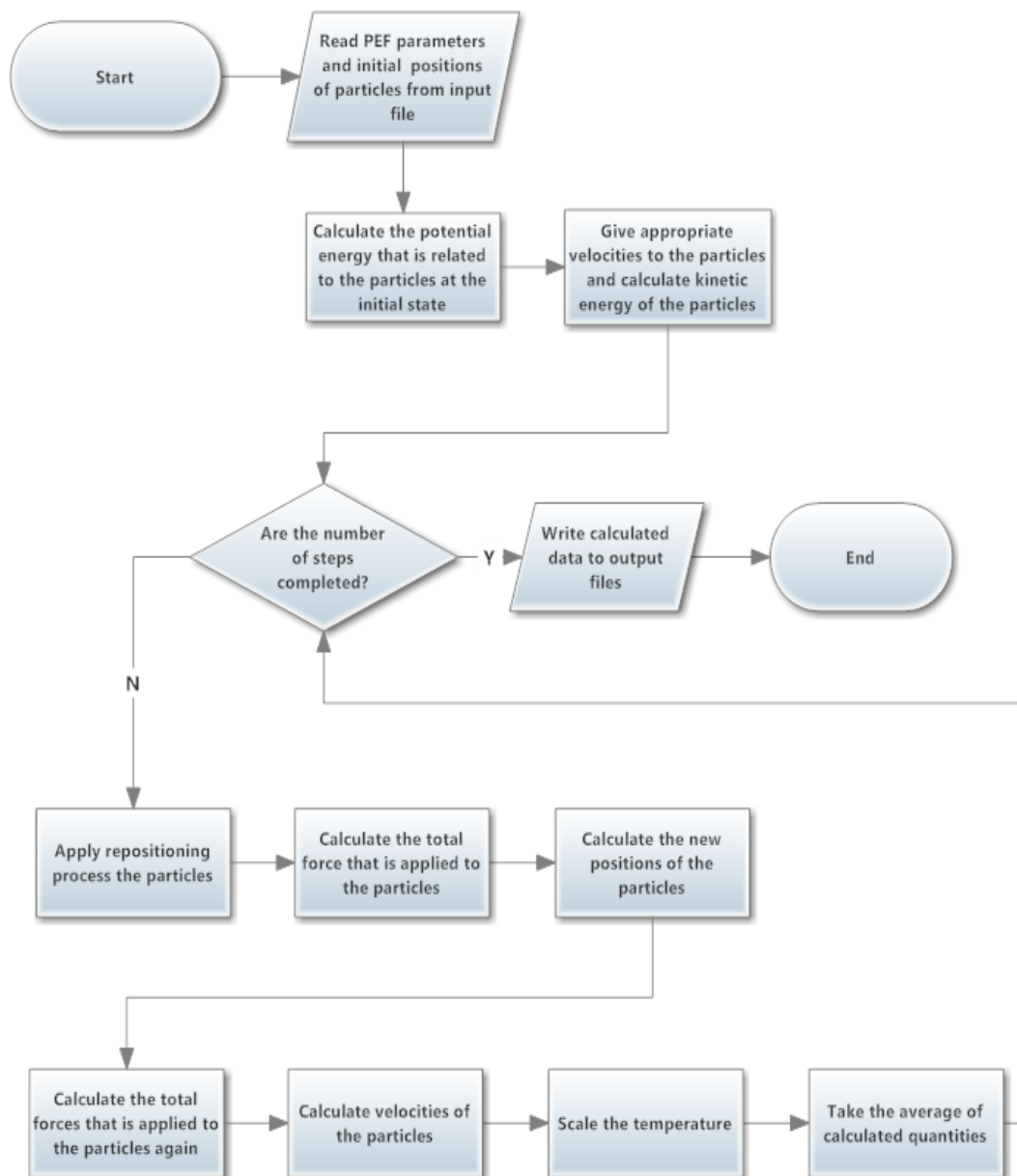


Figure 3: Simple flow diagram of the algorithm.

### 2.4.1. Parallelization

While the program finished the simulations for smaller models in a manner of hours, larger models took more than a week before the total energy graph converged to a local minimum. Because of this large number of simulations required to complete the study, the running time of the software had to be reduced by parallelization. The initial performance analysis of the code showed that approximately 92% of the CPU time was spent on the force calculations which were done twice for each MD step in the

main loop. The main cause of this workload is that this function calculates the forces acting on each atom in the system by solving the potential energy function for all the other atoms in the system. So the computational complexity of the program approaches  $\Theta(n^2)$ . In computer science,  $\Theta$  (big O) notation is used to classify algorithms by how they respond in their processing time or working space requirements to changes in input size. The notation characterizes functions according to their growth rates which is also referred to as order of the function.

The first version of the simulation program was written in FORTRAN and was running in a single thread. This caused the program to run at the same speed no matter what the number of CPU cores the system had. To better utilize the hardware resources, the program was parallelized firstly using the OpenMP library. OpenMP allowed the program to run the force function with parallel threads while a main thread executed the remaining code.

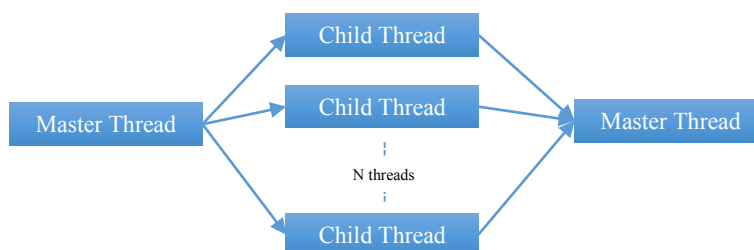


Figure 4: OpenMP execution flow diagram.

In this way, the force calculations for atoms were running in all the cores of the CPU. This allowed a 390% speed gain in a 4-core CPU. The OpenMP modification was done using compiler directives and without any code modification. Thus the results did not change with the first FORTRAN version. Using this procedure, similar MD simulation codes can easily be parallelized without making any changes in the program.

This allowed the simulations for small and medium sized models to finish in the required time but the models with more than 200 atoms still took more than 2 days to finish. To overcome this problem, the program has been rewritten in ANSI C++ and

the CUDA library has been used. CUDA is a parallel computing platform and enables increases in computing performance by harnessing the power of the graphics processing unit (GPU) [60]. In recent years, GPUs have evolved into highly parallel multi-core systems allowing very efficient manipulation of large blocks of data. This is due to the architectural difference between the CPU's and GPU's. While CPUs have powerful cores with limited numbers, GPUs have slower cores in a very large number. Nowadays, a middle range priced GPU has a minimum of 500 cores. This design is more effective than general-purpose CPUs for algorithms where processing of large blocks of data is done in parallel, such as: push-relabel maximum flow algorithm, fast sort algorithms of large lists, two-dimensional fast wavelet transform, and of course molecular dynamics simulations [61, 62, 63].



Figure 5: CPU and GPU architectures.

By running the new version of the CUDA-enabled C++ code, a simulation of 20,000,000 molecular dynamics steps that took 168.8 hours (7 days) for a large model consisting of 280 atoms, the total simulation time dropped to 61.3 hours (2 days). Further tests revealed that while simulations of larger models will take more than a month using a CPU, it will take less than a week for the GPU. With the increasing number of atoms in the model, the simulation time for the CPU increases logarithmically and the simulation time for the GPU increases linearly. This linear increase for the GPU continues until the GPU cores reach a saturation value which will not take place before the number of atoms reaches a thousand.

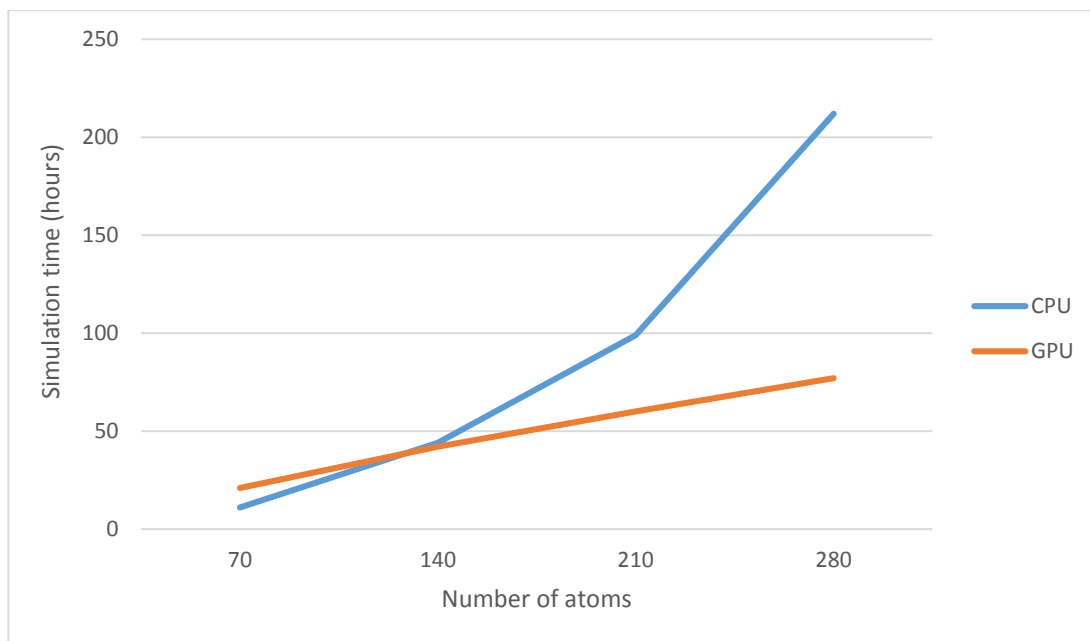


Figure 6: CPU vs GPU performance test results.

Simulations for the largest models (110-A) were completed using the C++ CUDA version of the program. The CUDA kernel code of the force function is given in Appendix B. The OpenMP parallelized version of the FORTRAN code is given in Appendix C. Sample input and output files for the code is given in Appendix D.



## CHAPTER 3

### RESULTS AND DISCUSSION

The first phase of the simulations was to repeat the MD steps using constant stress to remove the initial stresses of the systems. While the smaller models needed only a few ten thousands steps to reach equilibrium at 1 K, a minimum of 100,000 steps were repeated for each model to ensure finding the local minimum. The same models required more MD steps to reach equilibrium at 300 K than at 1 K. Larger models required more than 20,000,000 steps to reach equilibrium at 300 K. After the first relaxations, the systems were elongated by 5% by modifying the periodic boundary positions of the system and MD steps were repeated for the systems to reach equilibrium again with the new parameters. The completion of an elongation and relaxation process for a model will be called a strain step. The strain steps were repeated until fragmentation occurred along the nanowires. The following list shows three states for the nanowires. The first images are the relaxed states of the nanowires, the second images are states with the largest elongation, and the third images are the states after the breaking occurs. The images are presented with a view from the z axis which is the axis of the strain and a side view from the x axis which shows the length of the nanowire. The intermediate strain steps results for a particular model are displayed in the appendix.

#### **3.1. Cu(100) Nanowires**

The simulation results for copper nanowires generated along the (100) face are shown in this section.

### 3.1.1. Cu-100A at 1 K and 300 K

At 1 K, the crystal structure is preserved until strain step 5 (22% elongation). After strain step 5, the structure takes an amorphous form and continues to stretch until strain step 11 where necking occurs at the periodic boundaries. Along with the necking, some clustering occurred at center of the wire. The breaking occurred near the periodic boundary location after a 63% elongation. In total, 10 strain steps were applied to the nanowire. At each strain step, the system was relaxed with 100,000 MD steps.

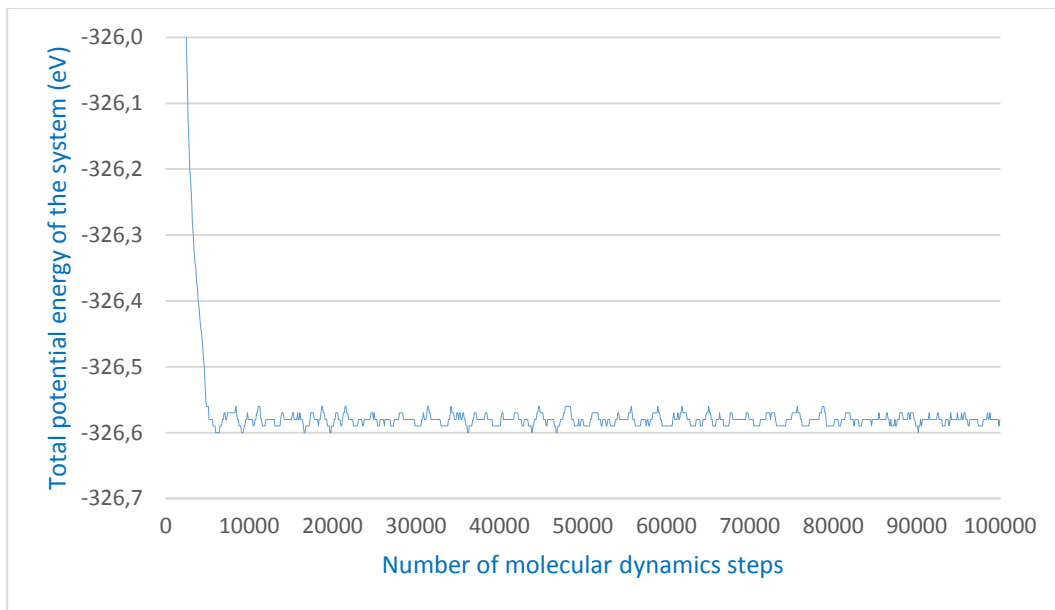


Figure 7: Total potential energy vs MD steps for Cu-100A at 1 K strain step 10.

When the temperature of the system was set at 300 K and the system was relaxed, the nanowire bent due to the formation of new bonds and the need for space of the crystal structure being suppressed at the periodic boundaries. In the following strain steps, the nanowire took a more straight form. The model preserved its crystal structure with little deformation even at strain step 14 at which point the wire was elongated 89%. This elongation is the longest one among all the simulations in this thesis. At this point a dislocation occurred at the middle of the wire and the broken wire formed a cluster with no apparent crystal structure. The clustering did not occur after the fragmentation in the simulation conducted at 1 K. At 300 K, a total of 15 strain steps were applied to the nanowire. After each strain step, 9,000,000 MD steps were performed to relax the system since the relaxation at 300 K took longer than at 1 K.

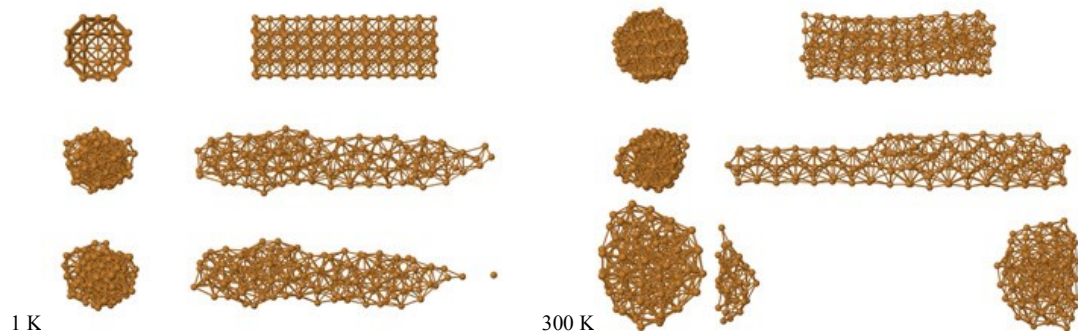


Figure 8: Cu-100A at 1 K and 300 K

### 3.1.2. Cu-100B at 1 K and 300 K

At 1 K, the structure could only stretch 2 strain steps resulting a 10% elongation. At the third step necking occurred and the nanowire broke. 2 strain steps were applied in total and 100,000 MD steps were performed to relax the system.

At 300 K the same model could stretch for 5 strain steps even though some clustering occurred at a region. Then the nanowire broke at the necking location after a 28% elongation. 5 strain steps were applied to the nanowire. At the first two steps, 5,000,000 MD steps were performed to relax the system but at the following steps, 9,000,000 MD steps were required for the system to relax.

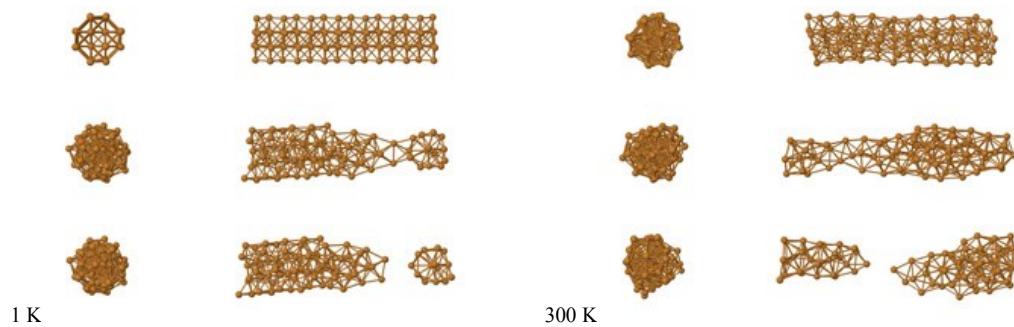


Figure 9: Cu-100B at 1 K and 300 K

### 3.1.3. Cu-100C at 1 K and 300 K

The model 100C has a very fragile initial form due to the lattice positions of the FCC model and the narrow size of the nanowire. But as the nanowire relaxed, the model took a more tubular form. At 1 K, the model stretched for 4 steps (16%) and broke near the periodic boundary. 100,000 MD steps were performed to relax the system. But at 300 K, due to the temperature, the system clustered and broke at the first relaxation without any strain applied. No strain steps could be applied at the model and 100,000 MD steps were performed to relax the system. The breaking of the nanowire can be seen from the graph with the sudden energy drop around MD step 10,000.

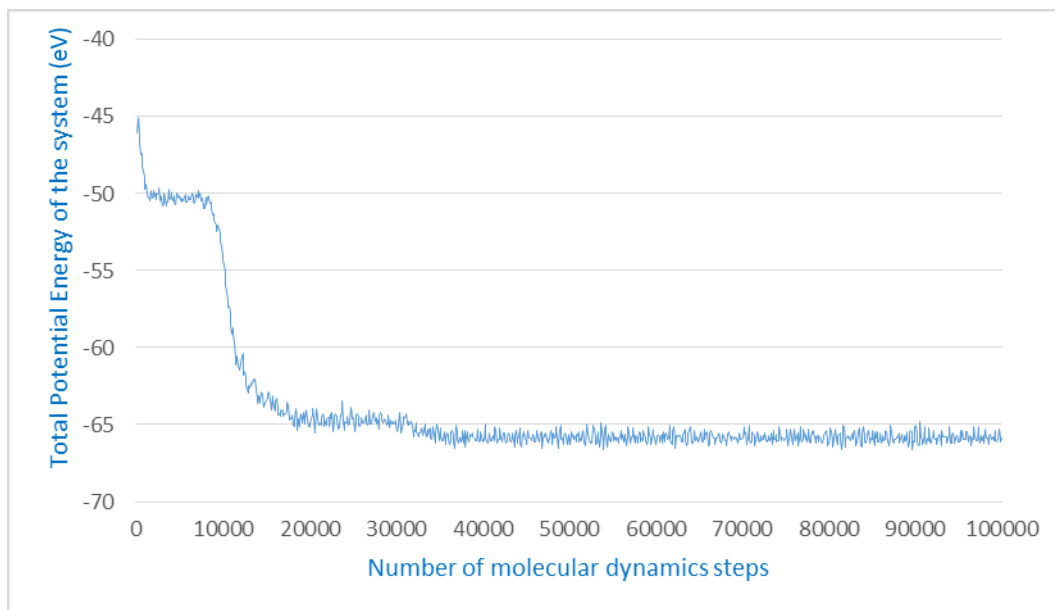


Figure 10: Total potential energy vs MD steps for Cu-100C at 300 K

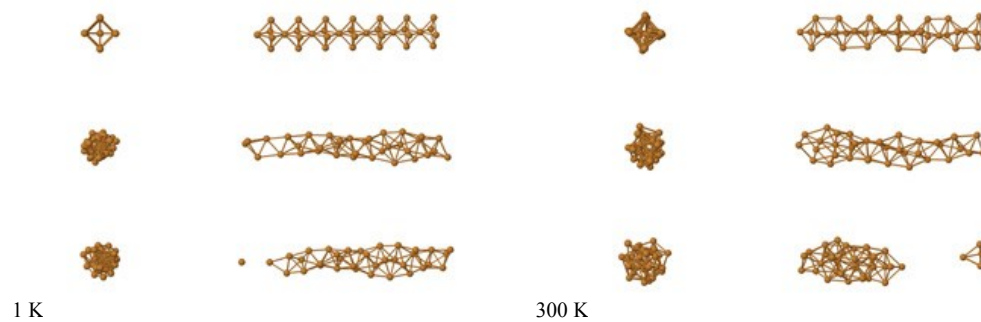


Figure 11: Cu-100C at 1 K and 300 K

### 3.2. Cu(110) Nanowires

The simulation results for copper nanowires generated along the (110) face are shown in this section.

#### 3.2.1. Cu-110A at 1 K and 300 K

In order to have a circular cross-section model, the 110A model had to be larger than the models of other Miller indices due to different lattice positions. Despite the larger cross-section size, 110A model did not show a behavior as ductile as the 100A model at 300 K but could stretch to same length at 1 K. While the model displayed a brittle fracture at 1 K and ductile fracture at 300 K, the final length that the model reached at both temperatures was the same 63% elongation at the 10<sup>th</sup> strain step. At both temperatures, the model preserved its crystal structure even with some clustering. While the system required 100,000 MD steps to relax at 1 K, it required 9,000,000 MD steps to relax at 300 K.

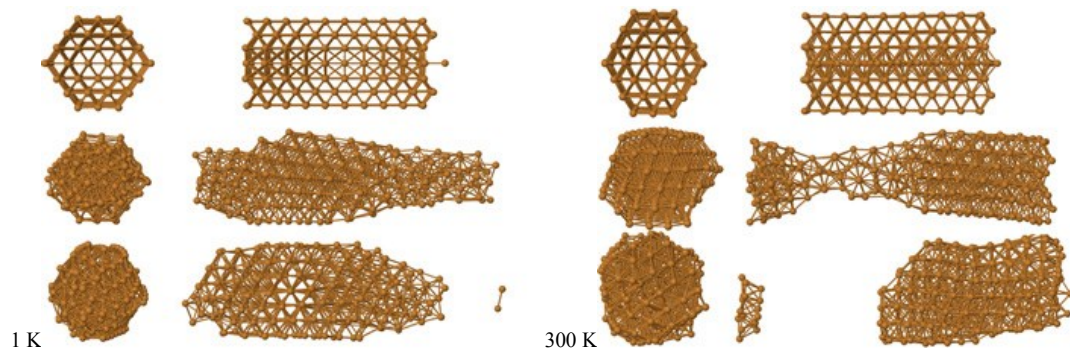


Figure 12: Cu-110A at 1 K and 300 K

#### 3.2.2. Cu-110B at 1 K and 300 K

For copper, 110B model was the most ductile of the medium sized models. Although some clustering occurred at 1 K, the model stretched until strain step 7 with an elongation of 41% where it broke at the periodic boundary. At 300 K, the model could stretch to same length as at 1 K, but it required more MD steps to relax. While a typical 100,000 MD steps were sufficient to relax the model at 1 K, the same model required 30,000,000 MD steps to relax at 300 K. The fracture at 300 K occurred at a necking location at one third of the nanowire. An interesting phenomena which occurred at this

model was that after stretching, the model took a spiral arrangement of atoms along the z-axis.

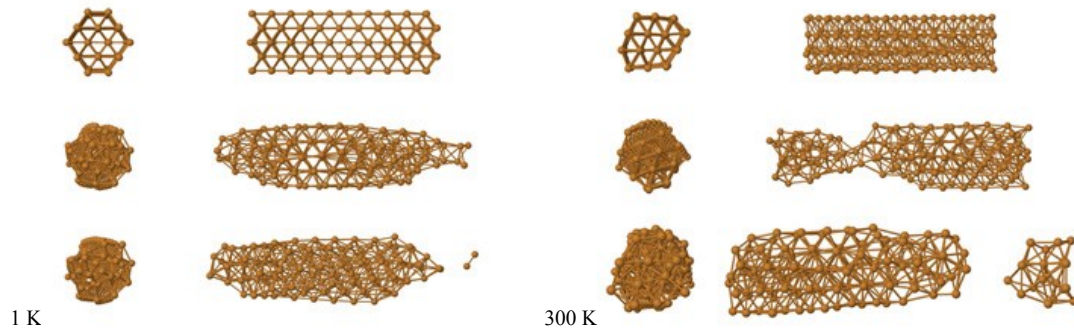


Figure 13: Cu-110B at 1 K and 300 K

### 3.2.3. Cu-110C at 1 K and 300 K

While forming circular cross-section models, the 110 face had the best lattice positions at the smallest size of the model. Due to the ideal initial structure of the model, the 110 face was the most ductile of the small models for all three materials. The model stretched for 7 strain steps for both cryo and room temperatures resulting a 41% elongation. The model broke near the periodic boundary with a brittle fracture at 1 K. The crystal structure was preserved. The fracture occurred at a necking point in a ductile fashion at 300 K after which some clustering occurred and the crystal structure was deformed. 3,000,000 MD steps were required to relax the system at 300 K and the typical 100,000 MD steps were sufficient to relax the model at 1 K.

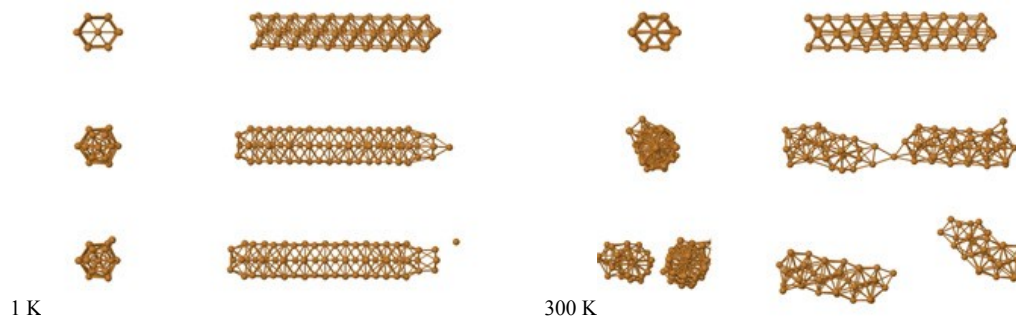


Figure 14: Cu-110C at 1 K and 300 K

### 3.3. Cu(111) Nanowires

The simulation results for copper nanowires generated along the (111) face are shown in this section.

#### 3.3.1. Cu-111A at 1 K and 300 K

The lattice positions for this model were very ideal for a round wire and formed a very ideal initial model. But the model was very brittle at 1 K and broke easily at the periodic boundary location at the fifth strain step with an elongation of 34%. The model was relatively more ductile at 300 K and stretched for 8 strain steps (48%) before breaking with a ductile fracture with two necking locations and with some clustering. After breaking, the wire cluttered. The 111 Miller indices was the least ductile for copper models. The model also required nearly 10,000,000 time steps to relax at each strain step at 300 K. The same model required only 100,000 time steps to relax at 1 K. While crystal structure was preserved at 1 K, no visible crystal structure was present at 300 K.

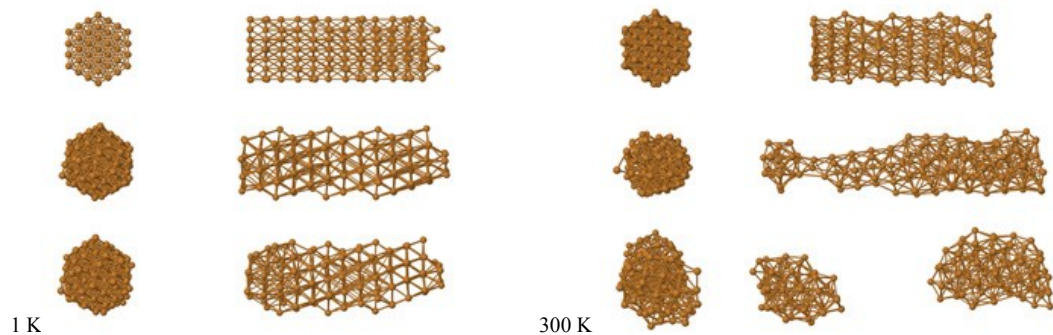


Figure 15: Cu-111A at 1 K and 300 K

#### 3.3.2. Cu-111B at 1 K and 300 K

Just like the 111A model, the smaller 111B model formed a very ideal initial model as a wire. But this face also was not very ductile at 1 K and broke at the third strain step (16% elongation). At 300 K, the wire stretched for two more strain steps and broke at 28% elongation. Both simulation resulted in brittle fractures. 5,000,000 MD steps were required to relax the model at 300 K. The crystal structure was preserved

at 1 K. An elastic deformation occurred at 300 K and after the fracture, the model regained its crystal structure arrangement.

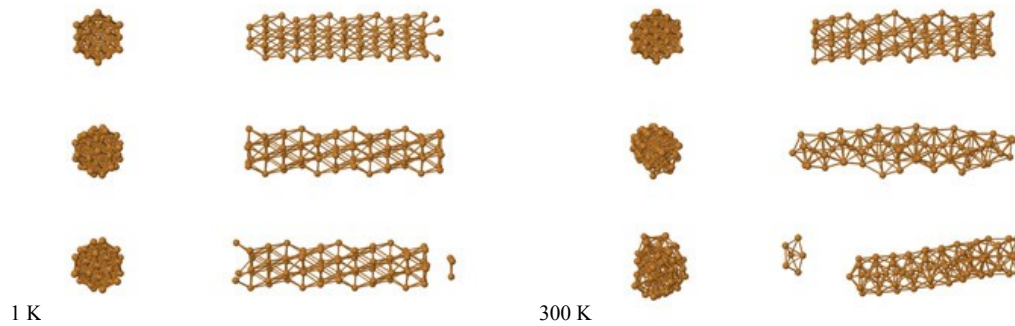


Figure 16: Cu 111B at 1 K and 300 K

### 3.3.3. Cu-111C at 1 K and 300 K

The initial form of the 111C model was very fragile at the beginning of the simulation with a single atom at each third atomic plane. But the model gained a tubular form after relaxation. Especially at 1 K, the model took a form similar to a nanotube. At 1 K the model broke after 2 strain steps at the periodic boundary location and took a square tubular form. At 300 K the model could not stretch and fractured at the first relaxation and clustered due to the high surface tension effect. Since the model clustered only 100,000 MD steps were performed at both temperatures.

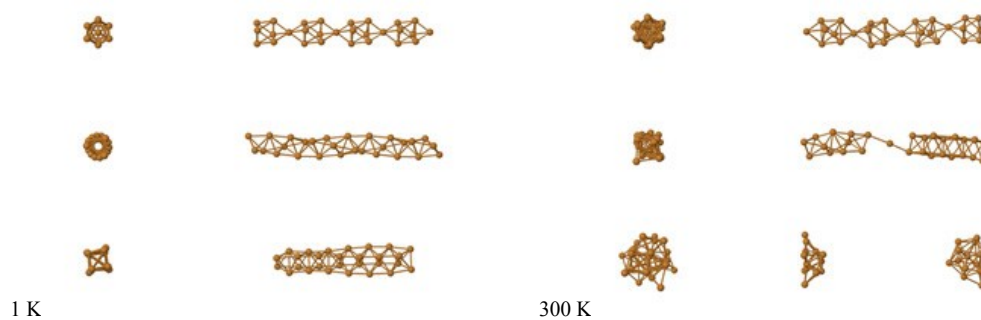


Figure 17: Cu 111C at 1 K and 300 K

### 3.4. Ag(100) Nanowires

The simulation results for silver nanowires generated along the (100) face are shown in this section.

#### 3.4.1. Ag-100A at 1 K and 300 K

At 1 K, the crystal structure of the model was very stable and could stretch until third strain step (16% elongation) without any deformation. Then the structure broke at the periodic boundary locations and suffered little clustering and preserved its crystal structure even at this point. At 300 K the model could stretch two times longer than at 1 K and could withstand 6 strain steps with local deformations and a single necking point at the center. At 34% elongation, the model suffered a ductile fracture with a monoatomic chain of four atoms before the fracture.

To relax the models after straining, 100,000 MD steps were sufficient at 1 K but at least 15,000,000 MD steps were necessary for the same model to relax at 300 K.

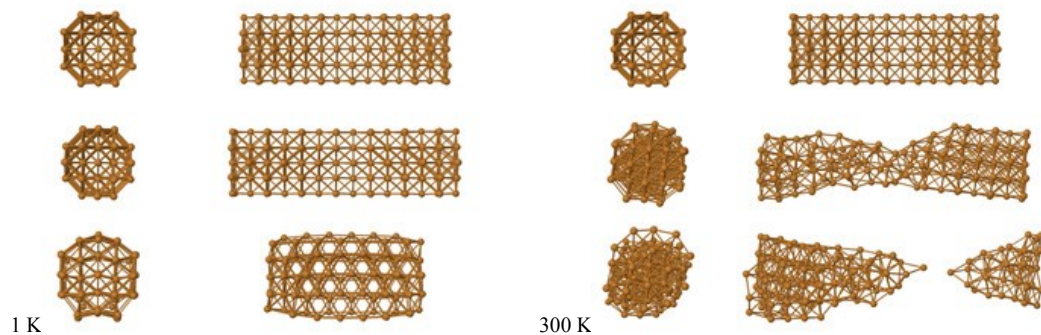


Figure 18: Ag 100A at 1 K and 300 K

#### 3.4.2. Ag-100B at 1 K and 300 K

The same fracture mechanisms of the Ag-100A model were apparent at this model at 1 K and the model stretched for 3 strain steps without any deformation and broke at this step after a 16% elongation. The model stretched for one less strain step with deformations at 300 K and broke and clustered and lost its crystal structure after a 10% elongation. While the model preserved its initial crystal structure at 1 K, it took a different form of crystal structure at 300 K.

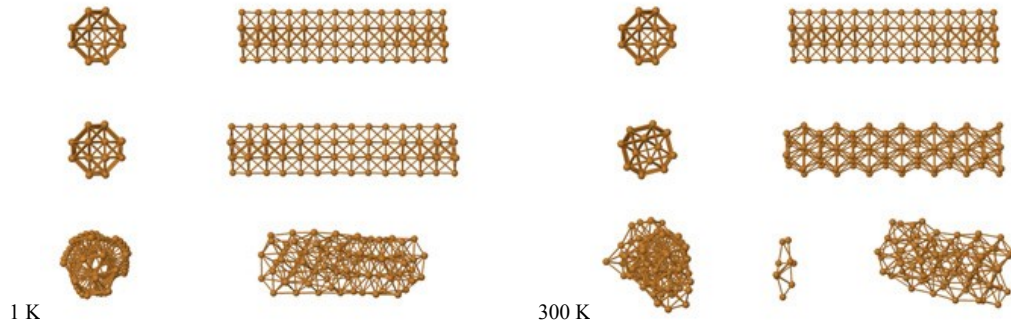


Figure 19: Ag 100B at 1 K and 300 K

### 3.4.3. Ag-100C at 1 K and 300 K

Relative to copper, the smaller 100C model was more ductile and could stretch 3 strain steps at 1 K (16% elongation) and 4 strain steps (22% elongation) at 300 K. The model took a form similar to a nanotube at both temperatures after relaxing.

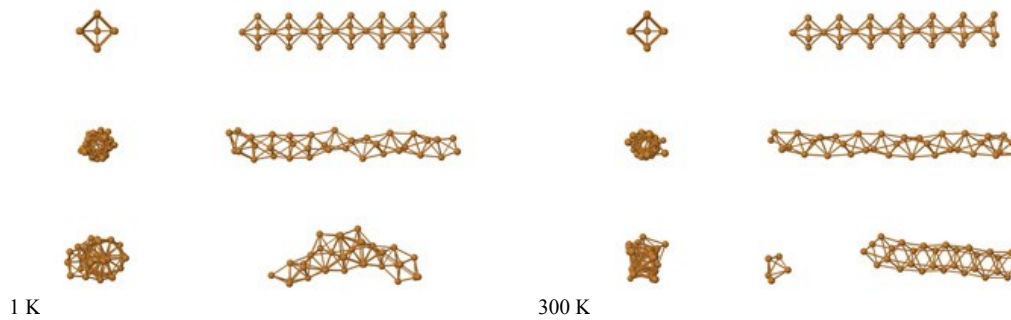


Figure 20: Ag 100C at 1 K and 300 K

## 3.5. Ag(110) Nanowires

The simulation results for Silver nanowires generated along the (110) face are shown in this section.

### 3.5.1. Ag-110A at 1 K and 300 K

The largest model of the simulations 110A was more ductile compared to 100A silver model but was not as ductile as the copper model. It stretched a 6 strain steps and broke at 34% at 1 K and stretched for 9 strain steps and broke at 55% at 300 K. The system preserved its crystal structure at 1 K but some local deformations and necking

at the center occurred at 300 K. This large model required 300,000 MD steps to relax at 1 K and 25,000,000 MD steps at 300 K.

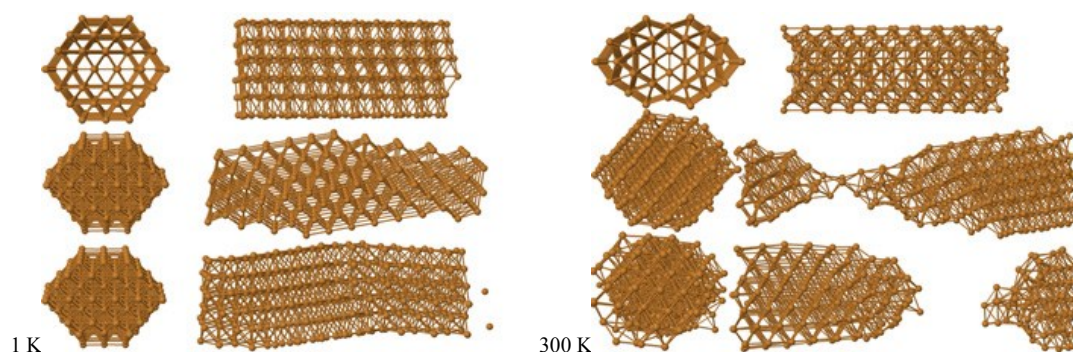


Figure 21: Ag 110A at 1 K and 300 K

### 3.5.2. Ag-110B at 1 K and 300 K

The 110B model was the most ductile for Ag compared to Cu and Au. The model could stretch for 6 strain steps at 1 K and 8 strain steps at 300 K and broke at 34% and 48% respectively. After the necking occurred, the model tended to form a crystal structure which is not aligned to z-axis and preserved this crystal structure after fracturing. The system required 300,000 MD steps to relax at 1 K and 22,000,000 MD steps to relax at 300 K.

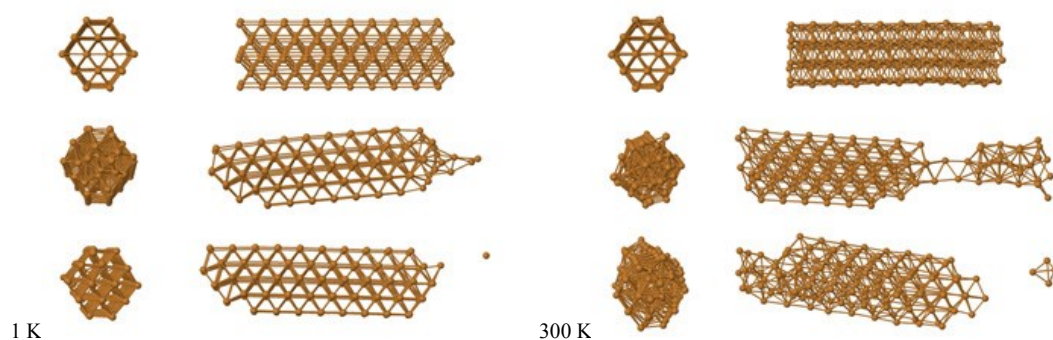


Figure 22: Ag 110B at 1 K and 300 K

### 3.5.3. Ag-110C at 1 K and 300 K

The model stretched without any crystal deformations and broke after 4 strain steps (22% elongation) at 1 K and 5 strain steps (28% elongation) at 300 K. The model

preserved its crystal structure at 1 K. The model suffered a very significant deformation at 300 K but still preserved its wire form. 8,000,000 MD steps were required to relax the model at 300 K which was the highest number for all three materials.

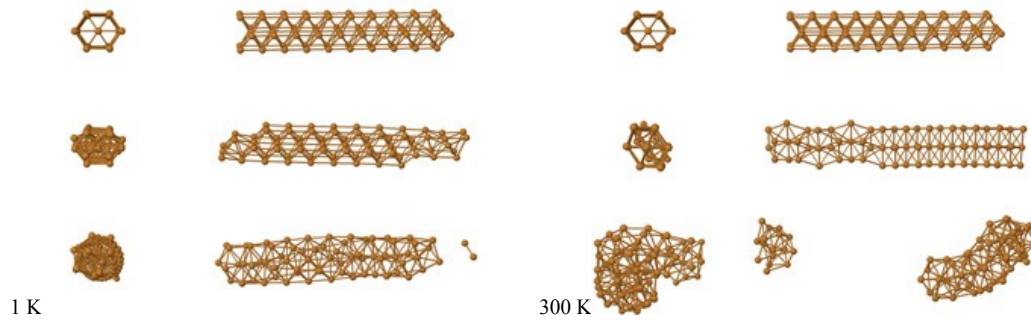


Figure 23: Ag 110C at 1 K and 300 K

### 3.6. Ag(111) Nanowires

The simulation results for silver nanowires generated along the (111) face are shown in this section.

#### 3.6.1. Ag-111A at 1 K and 300 K

Despite its large size, the model was very brittle at 1 K and broke at the periodic boundary locations after only 3 strain steps (16% elongation) while preserving its crystal structure. The model was the most ductile in all three simulated materials and could stretch for 10 strain steps with an elongation of 63% for silver. Some local clustering occurred at center of the model after strain step 8. 22,000,000 MD steps were performed to relax the system at 300 K.

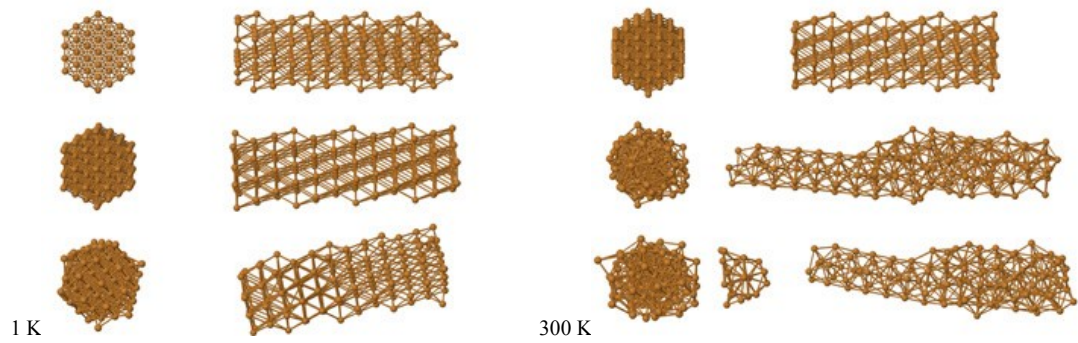


Figure 24: Ag 111A at 1 K and 300 K

### 3.6.2. Ag-111B at 1 K and 300 K

This model's ductility was equal for both temperatures and had brittle fractures at 3rd strain step with an elongation of 16%. 25,000,000 MD steps were required to relax the system at 300 K. Different from other models was that clustering occurred at 1 K but the initial form of the model was preserved at 300 K.

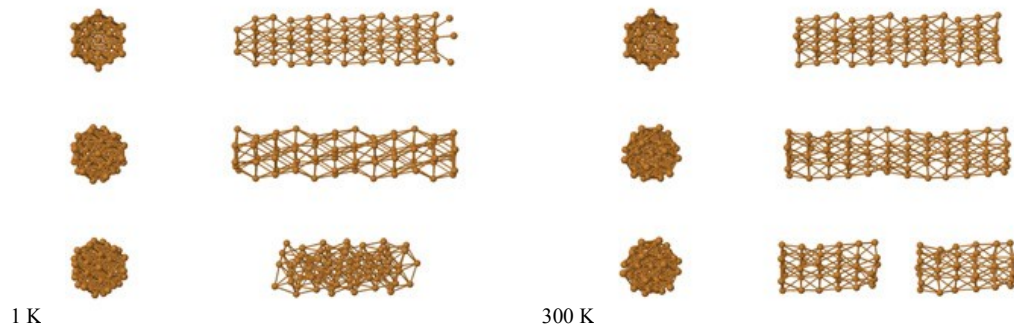


Figure 25: Ag 111B at 1 K and 300 K

### 3.6.3. Ag-111C at 1 K and 300 K

For both temperatures this model could only stretch for one strain step (5% elongation) and fractured at periodic boundary locations and clustered. Similar to the same model of the other materials, the model took a nanotube form after relaxation. 150,000 MD steps were performed to relax the system at 1 K and 3,000,000 MD steps were performed at 300 K. To better display the difference between the initial state and the relaxed state of the models, the first pictures in Figure 26 are the initial state and the second pictures are the relaxed state of the models.

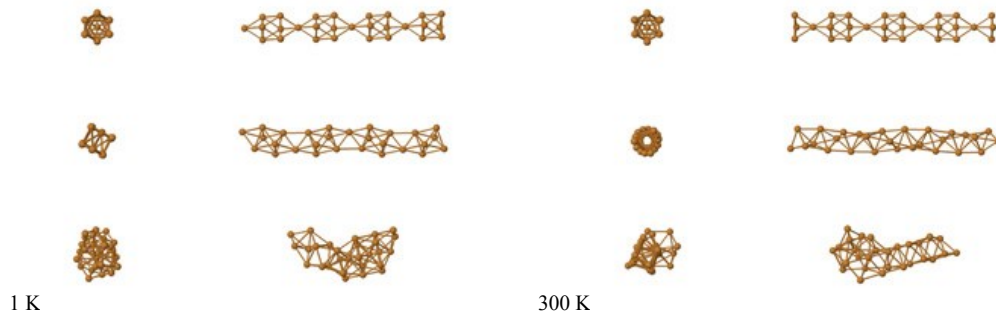


Figure 26: Ag 111C at 1 K and 300 K

### 3.7. Au(100) Nanowires

The simulation results for Gold nanowires generated along the (100) face are shown in this section.

#### 3.7.1. Au-100A at 1 K and 300 K

This model was not very ductile for Au compared to the materials Cu and Ag. At 1 K, the nanowire fractured at the 3rd strain step (16% elongation) and retracted. At 300 K, it fractured at the 4th strain step (22% elongation). The crystal structure was preserved at both temperatures and no clustering occurred. 10,000,000 MD steps were performed at 300 K and 100,000 MD steps were performed at 1 K for the system to reach equilibrium.

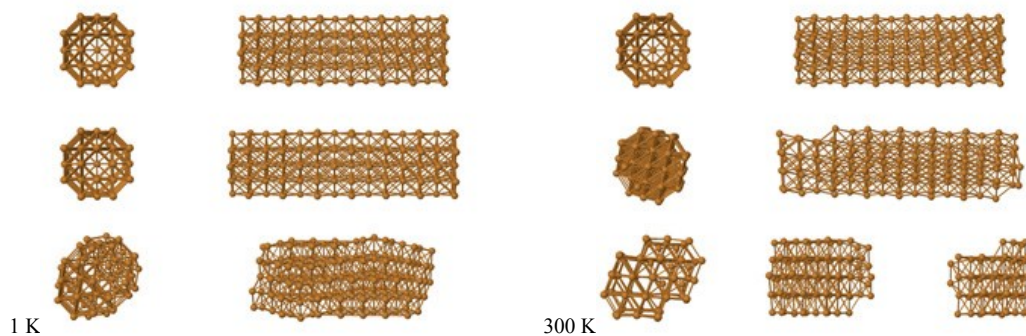


Figure 27: Au 100A at 1 K and 300 K

### 3.7.2. Au-100B at 1 K and 300 K

Fractures occurred at 3rd strain step (16% elongation) for both temperatures. The crystal structure was preserved and the wires retracted after the fracture without any clustering. 18,000,000 MD steps were performed at 300 K before the system reached equilibrium.

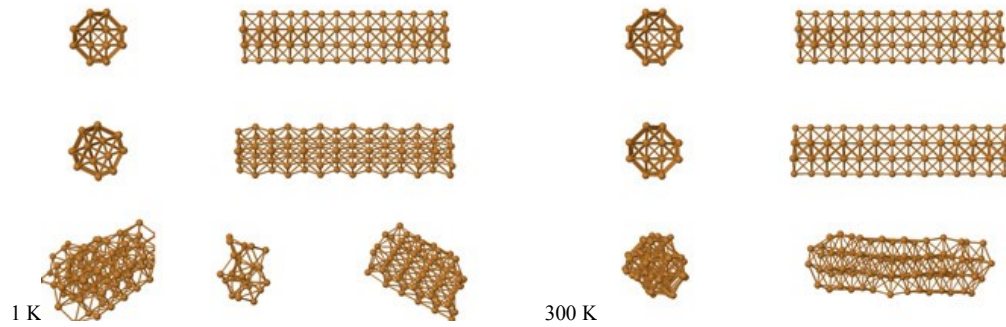


Figure 28: Au 100B at 1 K and 300 K

### 3.7.3. Au-100C at 1 K and 300 K

The model easily fractured at 1 K at the first strain step (5% elongation) but could stretch 3 strain steps (16%) at 300 K then broke without clustering. The model was not very stable at 1 K and required 200,000 MD steps to relax. 2,000,000 MD steps were performed at 300 K.

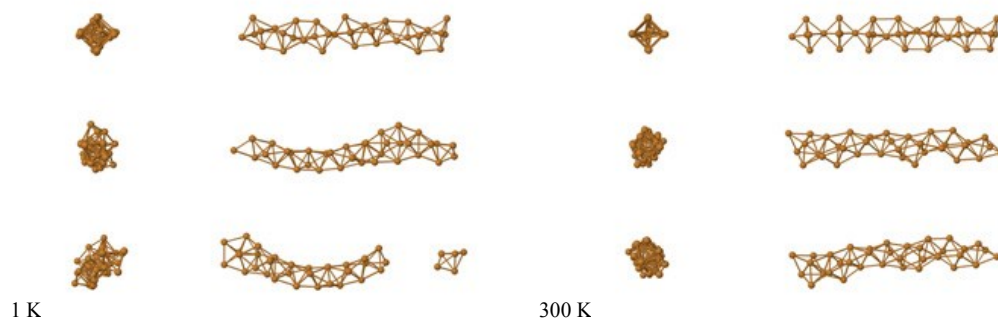


Figure 29: Au 100C at 1 K and 300 K

### 3.8. Au(110) Nanowires

The simulation results for gold nanowires generated along the (110) face are shown in this section.

#### 3.8.1. Au-110A at 1 K and 300 K

Like the other materials, these Miller indices was the most ductile for Au too. At 1 K the model took an interesting shape at the first relaxation and stretched until strain step 7 (41% elongation) and preserved its crystal structure after a brittle fracture near the periodic boundary location. At 300 K, the same model stretched until strain step 8 (48% elongation) and broke with some clustering but with a visible crystal orientation different from the orientation. The system required 20,000,000 MD steps at 300 K before reaching equilibrium.

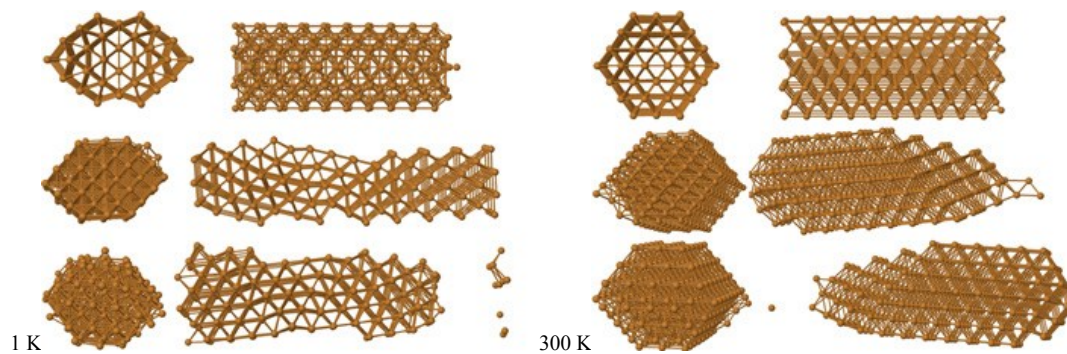


Figure 30: Au 110A at 1 K and 300 K

#### 3.8.2. Au-110B at 1 K and 300 K

After the first strain step, the model suffered fractures near periodic boundary locations and showed the same tendency as Ag to form a crystal lattice not aligned to the initial  $\langle 110 \rangle$  direction. The model broke at strain step 5 (28% elongation) and 6 (34% elongation) at 1 K and 300 K respectively. The system required 200,000 MD steps to reach equilibrium at 1 K and 18,000,000 MD steps at 300 K.

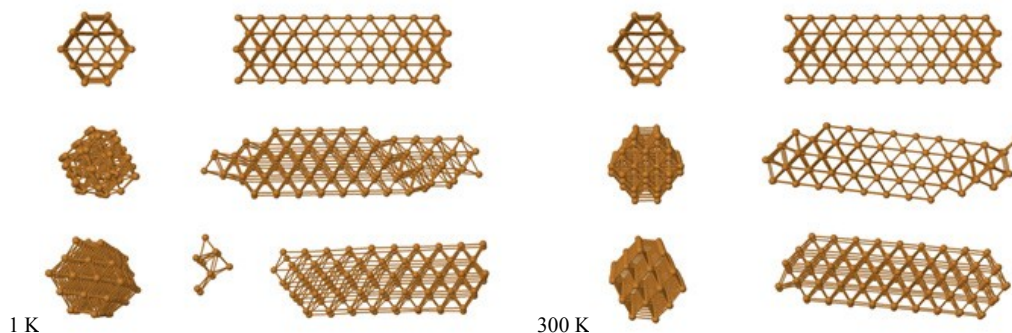


Figure 31: Au 110B at 1 K and 300 K

### 3.8.3. Au-110C at 1 K and 300 K

This model was relatively more stable for Au and could stretch for 4 strain steps (22% elongation) at 1 K and 6 strain steps (34% elongation) at 300 K. While the model preserved its crystal structure at 1 K, it gained a different crystal orientation at 300 K and lost its crystal structure after the fracture. The model was relatively stable at 300 K and required 6,000,000 MD steps to reach equilibrium.

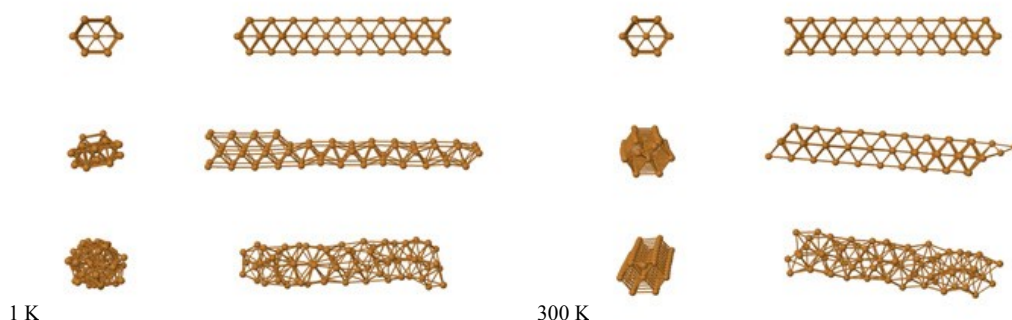


Figure 32: Au 110C at 1 K and 300 K

## 3.9. Au(111) Nanowires

The simulation results for gold nanowires generated along the (111) face are shown in this section.

### 3.9.1. Au-111A at 1 K and 300 K

The model broke at 1 K at step 4 (22% elongation) with a chain forming near the periodic boundary location. At 300 K the model broke at step 6 (34% elongation) with

a necking location at the center. No clustering occurred at both temperatures and the crystal structure was preserved. While 150,000 MD steps were performed for the system to reach equilibrium at 1 K, an average of 20,000,000 MD steps were performed at 300 K.

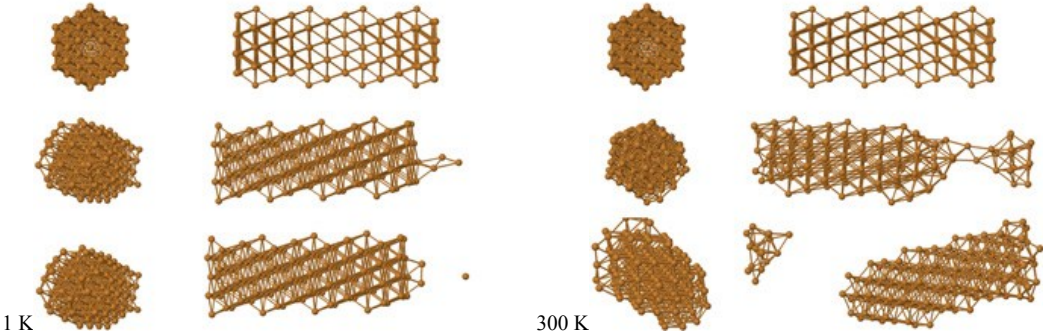


Figure 33: Au 111A at 1 K and 300 K

**3.9.2. Au-111B at 1 K and 300 K**

The model was very brittle at both temperatures and broke at the 2nd strain step (10% elongation). The brittle fracture occurred at the periodic boundary location at 300 K and near the periodic boundary location at 1 K. No deformations were present after the fracture at both temperatures. 15,000,000 MD steps were performed at 300 K.

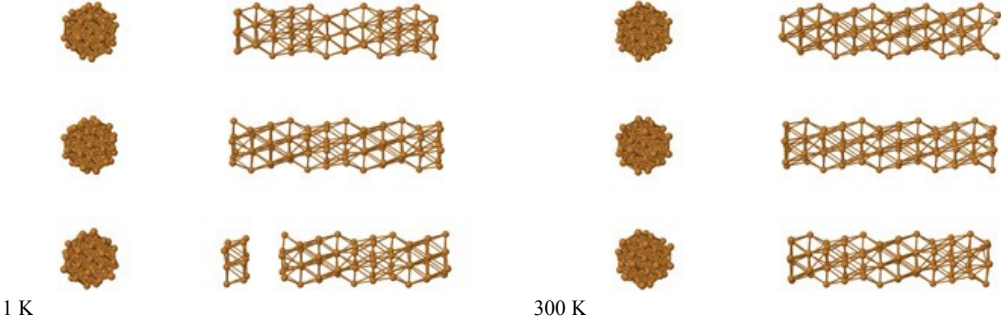


Figure 34: Au 111B at 1 K and 300 K

### 3.9.3. Au-111C at 1 K and 300 K

The model tended to cluster at both temperatures after breaking at the 1st strain step (5 % elongation). Unlike the other two materials, 111C model of gold did not take a nanotube form.

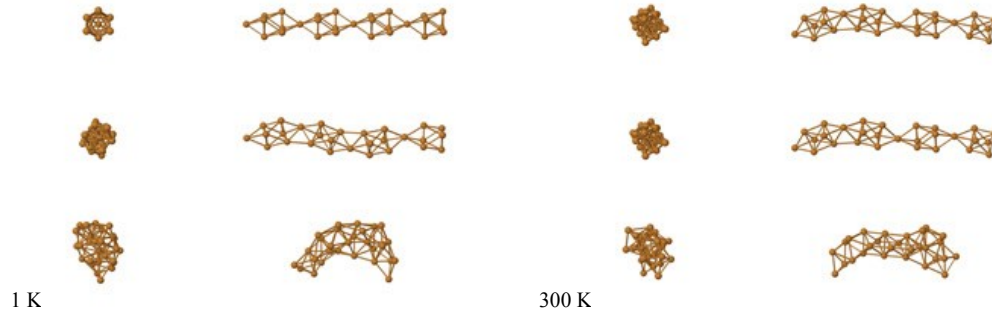


Figure 35: Au 111C at 1 K and 300 K

### 3.10. Energy graphics

Graphics for the elongation and total system energy changes of the nanowires are given in Figure 36 to Figure 41. Each color represents three different sized models (for example, 100-A, 100-B, 100-C). Therefore, each graph represents results for nine different models. The elongation values are calculated as percent change compared to the initial size of the nanorods. The energy changes are given as the amount of energy changes in the total energies of the systems compared to the initial relaxed state. The energies of the systems approach towards zero as the systems are stretched and the negative potential energy between the atoms decreases. As the nanowire breaks, the energy of the system suddenly drops because of the clustering of the atoms in the broken parts.

$E_0$  being the total energy of the system after the first relaxation,  $E_i$  is calculated as the total energy of the system after each strain step. So  $\Delta E$  in the graphics is calculated as  $E_i - E_0$  for each strain step and is shown in the graphics with respect to percent elongation obtained after the related strain step.

If we take  $L_0$  as the length of the nanowire at the initial configuration,  $L_i$  is calculated as the length of the nanowire after each strain step.

Then  $\Delta L$  is calculated as equation

$$\Delta L = \frac{L_i - L_0}{L_0} * 100 \quad (21)$$

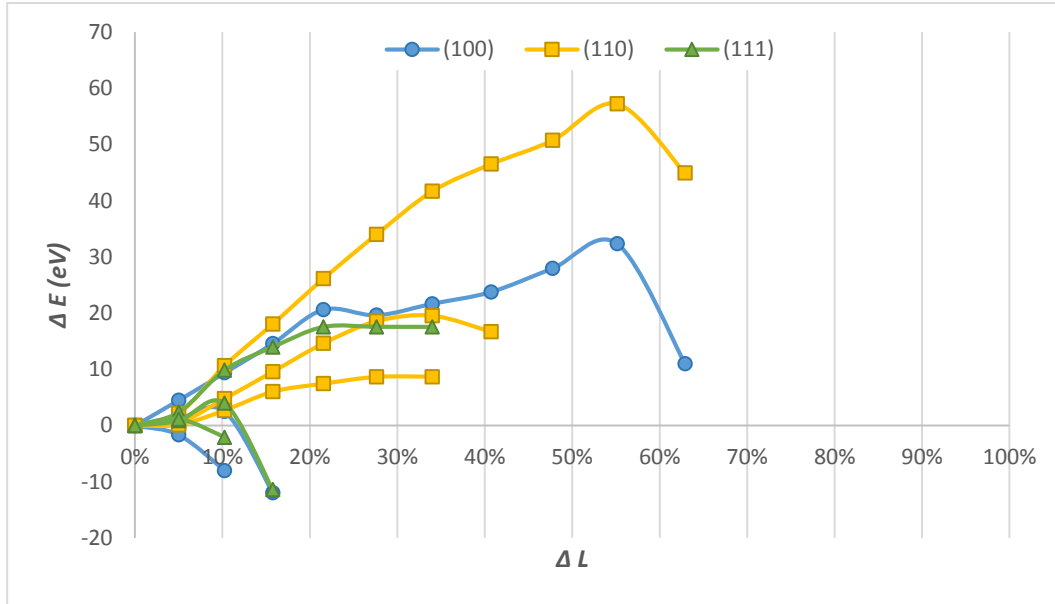


Figure 36: Strain energy with respect to elongation for different sizes of Cu nanowires at 1 K.

When looking at the strain energies for different sizes of Cu nanowires at 1 K, it is apparent that while the nanowire stretches, the negative potential energy between atoms decrease and the total energy of the system increases. The sudden drop at the end of the lines for largest models of (100) and (110) faces show that after the fracture of the nanowire, a high amount of clustering occurred. This sudden drop of energy is not present with the largest model of (111) face which shows that the nanowire did not cluster after fracturing. This result can also be seen from Figure 15 where the last image of the model shows a fractured but uncluttered nanowire.

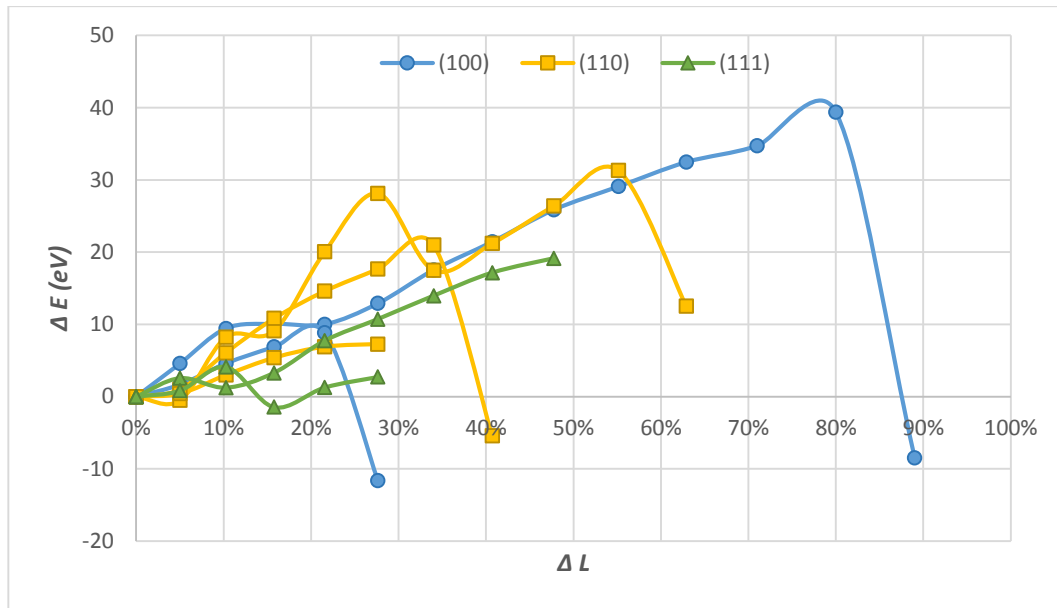


Figure 37: Strain energy with respect to elongation for different sizes of Cu nanowires at 300 K.

At 300 K, the energy drops after the fractures in the last strain steps is sharper than at 1 K. This shows that the clustering effect occurs more significantly at this temperature. Similar to results at 1 K, the (111) face does not form a cluster after the fractures. The energy data for the smallest model for (111) face is not visible in the graph due to its fracture at the initial relaxations. The only data for that model is the dot at the starting point of the graph. Except for the largest model of (100) face, models for (110) face are more resistant to strain and the models for (111) face are the least resistant to strain.

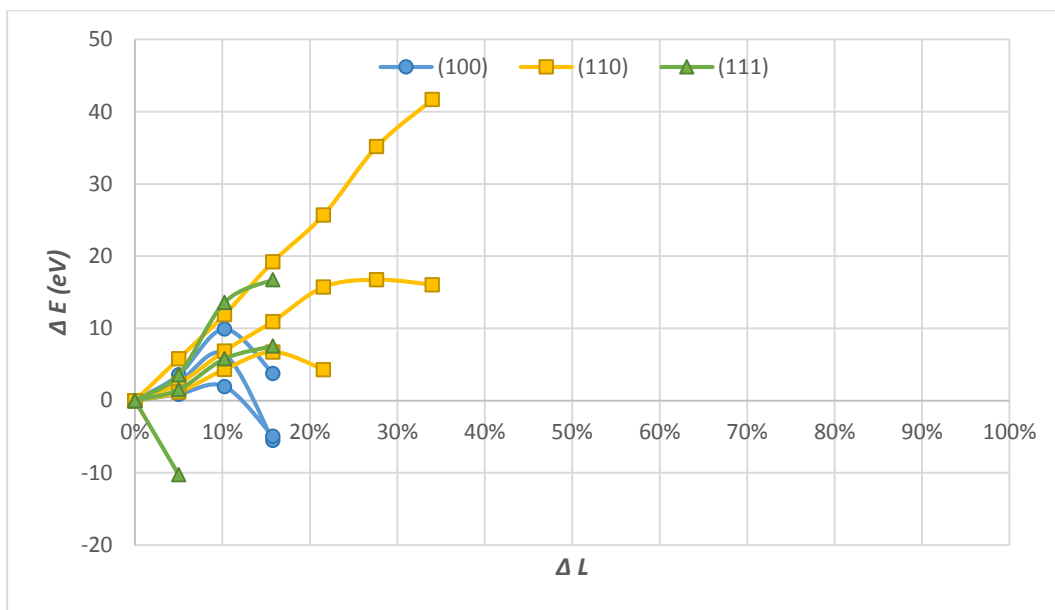


Figure 38: Strain energy with respect to elongation for different sizes of Ag nanowires at 1 K.

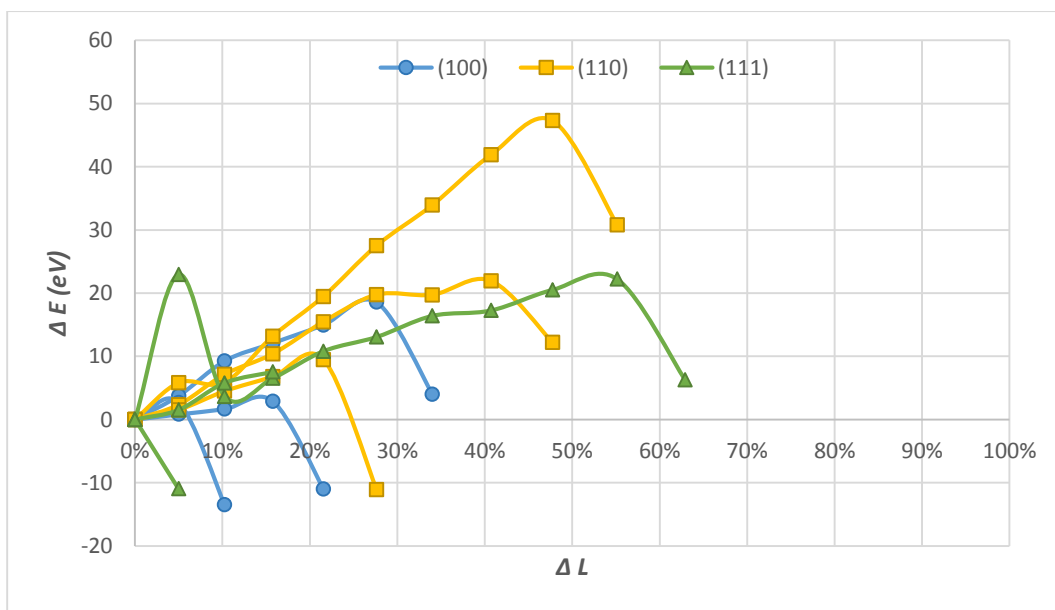


Figure 39: Strain energy with respect to elongation for different sizes of Ag nanowires at 300 K.

While the temperature had minimal effect to the strain capabilities of copper nanowires, it had a very significant effect on silver nanowires as visible in Figure 38 and Figure 39. At 1 K, the nanowires could not stretch more than 20% except for the

(110) face. Because of the small amount of stretching, almost no clustering occurred after the nanowires fractured. At 300 K, larger models could stretch more than 30% and the models heavily clustered after fracturing.

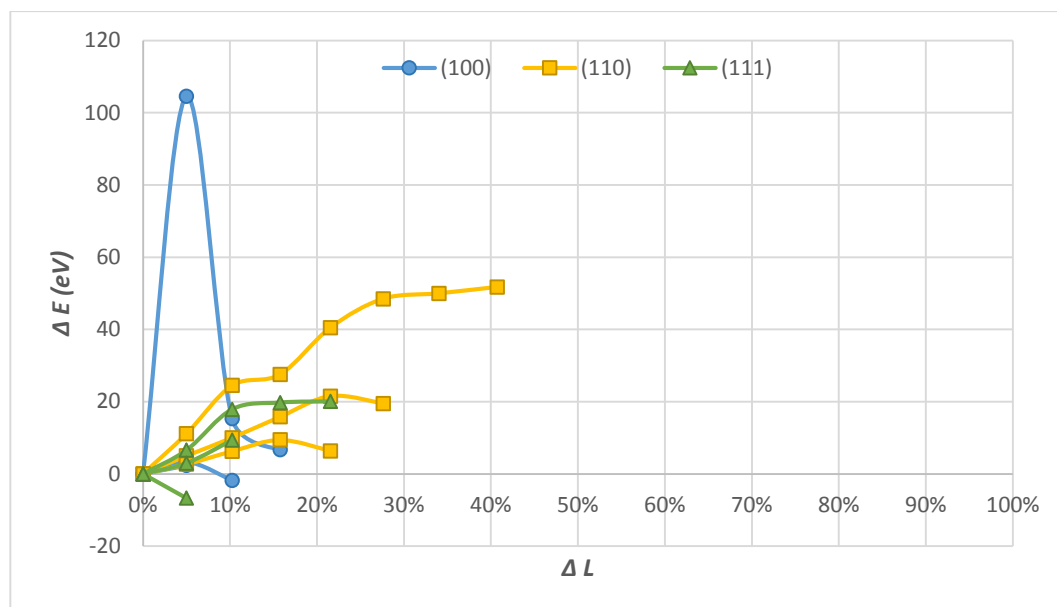


Figure 40: Strain energy with respect to elongation for different sizes of Au nanowires at 1 K.

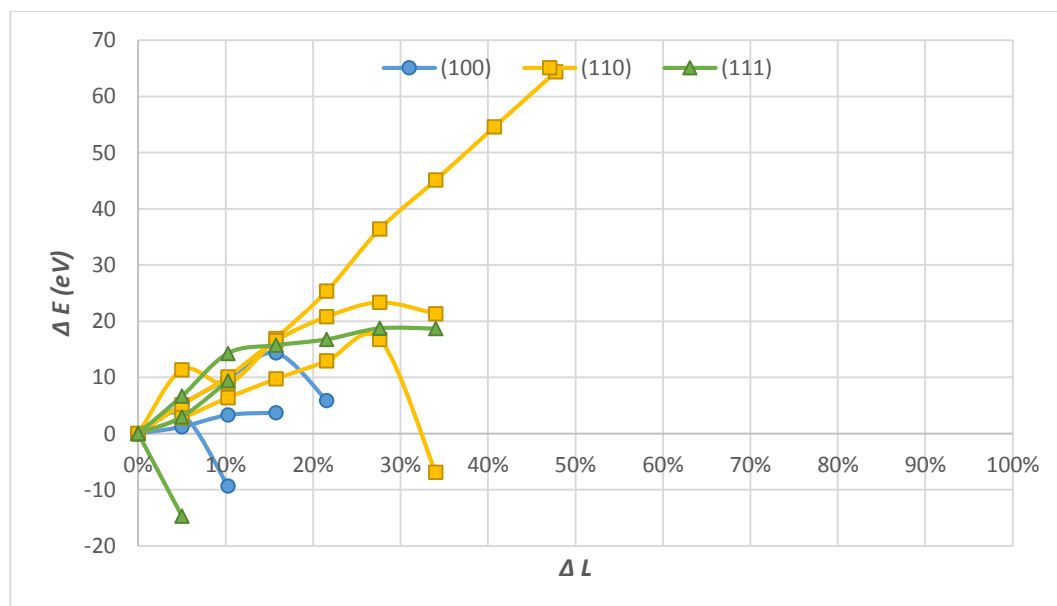


Figure 41: Strain energy with respect to elongation for different sizes of Au nanowires at 300 K.

Figure 40 and Figure 41 show the strain energies for gold nanowires. It is visible from the graphics that Au is the least ductile of the three materials simulated. Except from the (110) face, the nanowires could not stretch more than 20% at 1 K. The high peak of strain energy for the largest model of (100) face at 1 K show that the nanowire has stretched without any deformations and the total negative energy of the system is at its highest.

## CHAPTER 4

### CONCLUSIONS

For each simulation result, the mechanics of crystalline dislocation deformation due to strain was analyzed from the atomic structural rearrangements of the nanowires. In the conclusion section, the effect of the change in the width of the materials, the effect of the change in the temperature, the effect of the change in the crystal orientation, and the difference of ductility in different materials of the simulations will be evaluated.

When the nanowires are first allowed to relax without any strain, an initial tensile strength is present and the nanowires were bent along the z-axis. These initial tensile stresses were similarly observed in other works [33, 64]. The magnitude of these initial tensile stresses vary inversely with the proportion of surface atoms present in the nanowires.

For all three materials, the effect of the width is the most important parameter in the ductility of the nanowires. While the nanowires with 8 Å width (A models) have the most tendency to stretch without breaking, the smallest nanowires with 3-to-4 Å width (C models) do not stretch at all in most cases. While six of the C models could not stretch more than one strain step, only three of the models were ductile enough not to fracture before the fourth strain step. This is mainly due to the high ratio of surface atoms in the smaller nanowires. Surface atoms have relatively less interaction energy with respect to the bulk atoms. This, coupled with asymmetrical bonding of surface atoms with neighboring atoms, results in surface tension in restrained surfaces and surface contraction in unrestrained surfaces [33]. This results in a higher tendency to

fracture and to cluster in these small nanowires. As another effect of size, Koh and Lee reported in their work that since thermal induced disorder mainly affects the surface atoms, this effect was predominant in nanowires with diameters smaller than 5 Å, which have the largest proportion of surface atoms [33].

The change of temperature towards 300 K (room temperature) has a positive effect in the ductility of the materials. The materials stretch in an average 32% more at 300 K than 1 K in the simulations. It is well known for conventional FCC metals that, while their yield strength is insensitive to temperature and strain rate, their strain hardening is strongly temperature, and to a lesser extent, strain rate dependent. The uniform and efficient storage of dislocations leads to a high strain hardening rate at low temperatures. The main cause is the annihilation of dislocations through thermally activated cross slips. Another cause is the depression of climb at grain boundaries [65]. Another effect of temperature is the increased yield strength at lower temperatures. The effect is apparent in simulations for the Cu-111A model. While the crystal structure is preserved at 1 K, the same model suffers plastic deformations at 300 K. These simulation results are coherent with real experiments [65]. The effect is caused by a thermally activated deformation mechanism operative at room temperature and especially at slow strain rates, but not at lower temperatures.

Crystal orientations is also another important parameter for the nanowires in the amount of elongation before breaking. It has been shown that uni-axial strain shows cross-section geometry dependent characteristics. Nanowires which span the (110) face along the z-axis tend to have the most ductility for all the three metals while the (111) face is the most brittle. This is mainly due to the number of bonds between the planes being the least for the (111) face and the most for the (110). Also the gap between the planes is the largest for (111) plane. Another cause would be that that plastic elongation of a gold face-centered cubic crystal structure involves the sliding of (111) planes with respect to each other [66]. The transition states and energies for slip mechanisms have been determined in that work by Sorensen using the nudged elastic band method. A size-dependent crossover from a dislocation-mediated slip to a homogeneous slip is detected when the contact diameter becomes less than a few nm which is the case in our simulations.

As a conclusion, according to results of the present simulations, Cu nanowires seem to be more ductile, whereas Au nanowires seem to be more brittle with respect to the other materials studied in this work. These results could help future researches for metallic nanowire applications for their mechanical strength properties.

As a future work, more detailed study of the deformation mechanisms of the nanowires under strain could be conducted. Another interesting study could be to simulate the torsion effect on the same materials instead of strain effect. The molecular dynamics simulation study of the torsion effect could show interesting mechanical properties of these metals.



## REFERENCES

- [1] S. B. Heymsfield, Z. Wang, R. N. Baumgartner and R. Ross, "Human body composition: advances in models and methods.," *Annual review of nutrition*, vol. 17, pp. 527-58, 1997.
- [2] G. Cao, Synthesis, properties and applications, World Scientific, 2004.
- [3] H. Gleiter, "Nanostructured materials: State of the art and perspectives," *Nanostructured materials*, vol. 6, pp. 3--14, 1995.
- [4] H. Gleiter, "Nanostructured materials: basic concepts and microstructure," *Acta material*, no. 48, pp. 1--29, 2000.
- [5] V. V. Pokropivny and V. V. Skorokhod, "Classification of nanostructures by dimensionality and concept of surface forms engineering in nanomaterial science," *Materials Science and Engineering C*, no. 27, pp. 990-993, 2007.
- [6] A. P. Alivisatos, "Semiconductor clusters, nanocrystals, and quantum dots," *Science*, vol. 01, pp. 933--937, 1996.
- [7] T. Takagahara and T. Kyozauro, "Theory of the quantum confinement effect on excitons in quantum dots of indirect-gap materials," *Phys. Rev. B*, vol. 46, no. 23, pp. 15578-15581, 1992.
- [8] T. Vossmeier, L. Katsikas, M. Giersig, I. G. Popovic, K. Diesner, A. Chemseddine, A. Eychmueller and H. Weller, "CdS Nanoclusters: Synthesis, Characterization, Size Dependent Oscillator Strength, Temperature Shift of the Excitonic Transition Energy, and Reversible Absorbance Shift," *The Journal of Physical Chemistry*, vol. 31, no. 98, pp. 7665-7673, 1994.
- [9] J. W. Stouwdam and R. A. J. Janssen, "Red, green, and blue quantum dot LEDs with solution processable ZnO nanocrystal electron injection layers," *J. Mater. Chem.*, vol. 18, pp. 1889-1894, 2008.

- [10] W. Lee, S. H. Kang, J.-Y. Kim, G. B. Kolekar, Y.-E. Sung and S.-H. Han, "TiO<sub>2</sub> nanotubes with a ZnO thin energy barrier for improved current efficiency of CdSe quantum-dot-sensitized solar cells," *Nanotechnology*, vol. 20, no. 33, p. 335706, 2009.
- [11] V. Mokerov, Y. V. Fedorov, L. Velikovski and M. Y. Scherbakova, "New quantum dot transistor," *Nanotechnology*, vol. 12, no. 4, p. 552, 2001.
- [12] V. Ustinov, A. Zhukov, A. Kovsh, S. Mikhrin, N. Maleev, B. Volovik, Y. G. Musikhin, Y. M. Shernyakov, E. Y. Kondat'eva and M. Maximov, "Long-wavelength quantum dot lasers on GaAs substrates," *Nanotechnology*, vol. 11, no. 4, p. 397, 2000.
- [13] P. R. Van Tassel, "Nanotechnology in Medicine: Nanofilm Biomaterials," *The Yale journal of biology and medicine*, vol. 86, no. 4, p. 527, 2013.
- [14] D.-H. Kim, J.-H. Ahn, W. M. Choi, H.-S. Kim, T.-H. Kim, J. Song, Y. Y. Huang, Z. Liu, C. Lu and J. A. Rogers, "Stretchable and foldable silicon integrated circuits," *Science*, vol. 320, no. 5875, pp. 507--511, 2008.
- [15] T. Sekitani, Y. Noguchi, K. Hata, T. Fukushima, T. Aida and T. Someya, "A rubberlike stretchable active matrix using elastic conductors," *Science*, vol. 321, no. 5895, pp. 1468-1472, 2008.
- [16] J. A. Rogers, T. Someya and Y. Huang, "Materials and Mechanics for Stretchable Electronics," *Science*, no. 327, p. 1603, 2010.
- [17] J. N. Tiwari, R. N. Tiwari and K. S. Kim, "Zero-dimensional, one-dimensional, two-dimensional and three-dimensional nanostructured materials for advanced electrochemical energy devices," *Progress in Materials Science*, vol. 57, no. 4, pp. 724-803, 2012.
- [18] B. Wang, S. Yin, G. Wang, A. Buldum and J. Zhao, "Novel Structures and Properties of Gold Nanowires," *Phys. Rev. Lett.*, vol. 86, no. 10, pp. 2046-2049, 2001.
- [19] K. Takei, T. Takahashi, J. C. Ho, H. Ko, A. G. Gillies and R. S. F. & A. J. Paul W. Leu, "Nanowire active-matrix circuitry for low-voltage macroscale artificial skin," *Nature Materials*, vol. 9, p. 821–826, 2010.

- [20] C. Q. Chen, Y. Shi, Y. S. Zhang, J.-L. Zhu and Y. J. Yan, "Size Dependence of Young's Modulus in ZnO Nanowires," *Phys. Rev. Lett.*, vol. 96, no. 7, p. 075505, 2006.
- [21] X. Wang, J. Zhou, Song, J. Liu, N. Xu and Z. L. Wang, "Piezoelectric Field Effect Transistor and Nanoforce Sensor Based on a Single ZnO Nanowire," *Nano Letters*, vol. 6, no. 12, pp. 2768-2772, 2006.
- [22] W. Liang, M. Zhou and F. Ke, "Shape Memory Effect in Cu Nanowires," *Nano Letters*, vol. 5, no. 10, pp. 2039-2043, 2005.
- [23] S. Lu and B. Panchapakesan, "Hybrid platinum/single-wall carbon nanotube nanowire actuators: metallic artificial muscles," *Nanotechnology*, vol. 17, no. 3, p. 888, 2006.
- [24] D. R. Bowler, "Atomic-scale nanowires: physical and electronic structure," *Journal of Physics: Condensed Matter*, vol. 16, no. 24, p. R721, 2004.
- [25] E. D. Haberer, J. H. Joo, J. F. Hodelin and E. L. Hu, "Enhanced photogenerated carrier collection in hybrid films of bio-templated gold nanowires and nanocrystalline CdSe," *Nanotechnology*, vol. 20, no. 41, p. 415206, 2009.
- [26] H. J. Parab, H. M. Chen, T.-C. Lai, J. H. Huang, P. H. Chen, R.-S. Liu, M. Hsiao, C.-H. Chen, D.-P. Tsai and Y.-K. Hwu, "Biosensing, Cytotoxicity, and Cellular Uptake Studies of Surface-Modified Gold Nanorods," *The Journal of Physical Chemistry C*, no. 113, pp. 7574-7578, 2009.
- [27] E. Fourkal, I. Velchev, A. Taffo, C. Ma, V. Khazak and N. Skobeleva, "Photo-Thermal Cancer Therapy Using Gold Nanorods," *World Congress on Medical Physics and Biomedical Engineering, IFMBE Proceedings*, no. 25, pp. 761--763, 2009.
- [28] R. Zhu, C.-H. Chung, K. C. Cha, W. Yang, Y. B. Zheng, H. Zhou, T.-B. Song, C.-C. Chen, P. S. Weiss, G. Li and Y. Yang, "Fused Silver Nanowires with Metal Oxide Nanoparticles and Organic Polymers for Highly Transparent Conductors," *ACS Nano*, vol. 5, no. 12, pp. 9877-9882, 2011.
- [29] C. Chappert, A. Fert and F. N. Van Dau, "The emergence of spin electronics in data storage.," *Nature materials*, vol. 6, no. 11, pp. 813--823, 2007.

- [30] D. Kharat, H. Muthurajan and B. Praveenkumar, "Present and Futuristic Military Applications of Nanodevices," *Synthesis and Reactivity in Inorganic, Metal-Organic, and Nano-Metal Chemistry*, vol. 36, no. 2, pp. 231--235, 2006.
- [31] E. C. Walter, R. M. Penner, H. Liu, K. H. Ng, M. P. Zach and F. Favier, "Sensors from electrodeposited metal nanowires," *Surf. Interface Anal.*, vol. 34, p. 409–412, 2002.
- [32] D. Natelson, R. Willett, K. West and L. Pfeiffer, "Fabrication of extremely narrow metal wires," *Applied Physics Letters*, vol. 77, no. 13, pp. 1991-1993, 2000.
- [33] S. J. A. Koh and H. P. Lee, "Molecular dynamics simulation of size and strain rate dependent mechanical response of FCC metallic nanowires," *Nanotechnology*, vol. 17, no. 14, p. 3451, 2006.
- [34] S.-P. Ju, J.-S. Lin and W.-J. Lee, "A molecular dynamics study of the tensile behaviour of ultrathin gold nanowires," *Nanotechnology*, vol. 15, no. 9, p. 1221, 2004.
- [35] J. D. Dunn, K. Gall and L. Martin, "Atomistic simulation of the structure and elastic properties of gold nanowires," *Journal of the Mechanics and Physics of Solids*, vol. 52, no. 9, pp. 1935--1962, 2004.
- [36] J.-W. K. Hwang and Ho-Jung, "Mechanical deformation study of copper nanowire using atomistic simulation," *Nanotechnology*, vol. 12, no. 3, p. 295, 2001.
- [37] H. Wu, "Molecular dynamics study on mechanics of metal nanowire," *Mechanics Research Communications*, vol. 33, no. 1, pp. 9-16, 2006.
- [38] P. D. Haynes, *Linear-scaling methods in ab initio quantum-mechanical calculations*, University of Cambridge, 1998.
- [39] C. Froese Fischer, "General Hartree-Fock program," *Computer physics communications*, vol. 43, no. 3, pp. 355--365, 1987.
- [40] M. H. N. Assadi and D. A. Hanaor, "Theoretical study on copper's energetics and magnetism in TiO<sub>2</sub> polymorphs," *Journal of Applied Physics*, vol. 113, no. 23, p. 233193, 2013.

- [41] Ş. Erkoç, Lecture notes on simulations of many-particle systems, METU, (Unpublished), 2004.
- [42] Ş. Erkoç, *Lecture notes on Introduction to Nanoscience and Nanotechnology*, Ankara: Unpublished, 2006.
- [43] I.-L. Chang and Y.-C. Chen, "Is the molecular statics method suitable for the study of nanomaterials? A study case of nanowires," *Nanotechnology*, vol. 18, no. 31, p. 315701, 2007.
- [44] M. T. Dove, *Introduction to lattice dynamics*, vol. 4, Cambridge university press, 1993.
- [45] M. T. Dove, "An introduction to atomistic simulation methods," *Seminarios de la SEM*, vol. 4, pp. 7--37, 2008.
- [46] D. C. Rapaport, *The art of molecular dynamics simulation*, Cambridge: Cambridge university press, 2004.
- [47] J. Murrell, S. Carter, S. Farantos, P. Huxley and A. Varandas, "Molecular Potential Energy Functions," *Wiley*, 1984.
- [48] Ş. Erkoç, "Empirical many-body potential energy functions used in computer simulations of condensed matter properties," *Physics Reports*, vol. 278, no. 2, pp. 79--105, 1997.
- [49] L. Verlet, "Computer experiments on classical fluids. I. Thermodynamical properties of Lennard-Jones molecules," *Physical review*, vol. 159, no. 1, p. 98, 1967.
- [50] J. M. Haile, *Molecular dynamics simulation: elementary methods*, Wiley, 1992.
- [51] G. Ciccotti and W. G. Hoover, *Molecular-dynamics simulation of statistical-mechanical systems*, North-Holland Amsterdam, 1986.
- [52] M. D. Morse, "Clusters of transition-metal atoms," *Chemical Reviews*, vol. 86, no. 6, pp. 1049-1109, 1986.
- [53] P. Schofield, "Computer simulation studies of the liquid state," *Computer Physics Communications*, vol. 5, no. 1, pp. 17-23, 1973.

- [54] S. L. Roux, "Interactive Structure Analysis of Amorphous and Crystalline Systems program," Central Michigan University, 22 2 2012. [Online]. Available: <http://isaacs.sourceforge.net/phys/pbc.html>. [Accessed 31 5 2014].
- [55] Ş. Erkoç, "An empirical many-body potential energy function constructed from pair-interactions," *Zeitschrift für Physik D: Atoms, Molecules and Clusters*, vol. 32, no. 3, pp. 257--260, 1994.
- [56] Ş. Erkoç, "Empirical potential energy functions used in the simulations of materials properties," *Annual Reviews of Computational Physics*, vol. 9, pp. 1--103, 2001.
- [57] Ş. Erkoç, "Structural Stability and Energetics of FCC Metal Microclusters. Empirical Many-Body Potential Energy Function Calculation," *physica status solidi (b)*, vol. 161, no. 1, pp. 211--216, 1990.
- [58] B. Wang, S. Yin, G. Wang, A. Buldum and J. Zhao, "Novel Structures and Properties of Gold Nanowires," *Phys. Rev. Lett.*, vol. 86, no. 10, pp. 2046--2049, 2001.
- [59] "Jmol: an open-source Java viewer for chemical structures in 3D," [Online]. Available: <http://www.jmol.org>.
- [60] NVidia, "NVIDIA CUDA parallel computing platform," NVidia, 1 6 2014. [Online]. Available: <http://developer.nvidia.com>. [Accessed 1 6 2014].
- [61] J. A. Anderson, C. D. Lorenz and A. Travesset, "General purpose molecular dynamics simulations fully implemented on graphics processing units," *Journal of Computational Physics*, vol. 227, no. 10, pp. 5342--5359, 2008.
- [62] W. Liu, B. Schmidt, G. Voss and W. Müller-Wittig, "Accelerating molecular dynamics simulations using Graphics Processing Units with CUDA," *Computer Physics Communications*, vol. 9, no. 9, pp. 634-341, 2008.
- [63] W. Liu, B. Schmidt, G. Voss and W. Müller-Wittig, "Molecular dynamics simulations on commodity GPUs with CUDA," in *High Performance Computing – HiPC 2007*, Springer Berlin Heidelberg, 2007, pp. 185-196.
- [64] B. G. FINBOW, R. L.-B. MCDONALD and IR, "Atomistic simulation of the stretching of nanoscale metal wires," *Molecular Physics*, vol. 92, no. 4, pp. 705-714, 2010.

- [65] Y. Wang and E. Ma, "Temperature and strain rate effects on the strength and ductility of nanostructured copper," *Applied physics letters*, vol. 83, no. 15, pp. 3165--3167, 2003.
- [66] M. R. Sorensen, M. Brandbyge and K. W. Jacobsen, "Mechanical deformation of atomic-scale metallic contacts: structure and mechanisms," *Physical Review B*, vol. 57, no. 6, p. 3283, 1998.
- [67] C. Kittel, *Introduction to Solid State Physics*, Sixth ed., New York: John Wiley and Sons, 1986.



## APPENDIX A

### UNIT CELLS TO GENERATE NANOROD MODELS

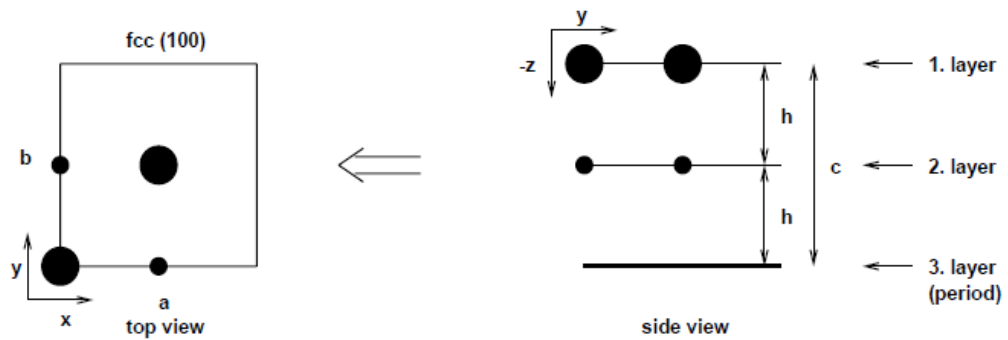


Figure 42: Unit cell to generate face centered (100) surface.

The relation between lattice constant ( $a_0$ ) and nearest neighbor distance ( $d_{nn}$ ) for the FCC crystal, the unit cell sizes in terms of lattice constant ( $a_0$ ), and the interlayer spacing ( $h$ ) are defined as in equation (22) below and are taken from [41]. The lattice constant ( $a_0$ ) values for the studied elements are: 3.61 Å for copper, 4.09 Å for silver and 4.08 Å for gold [67].

$$a_0 = \sqrt{2}d_{nn} , \quad a = b = c = a_0 , \quad h = \frac{1}{2}a_0 \quad (22)$$

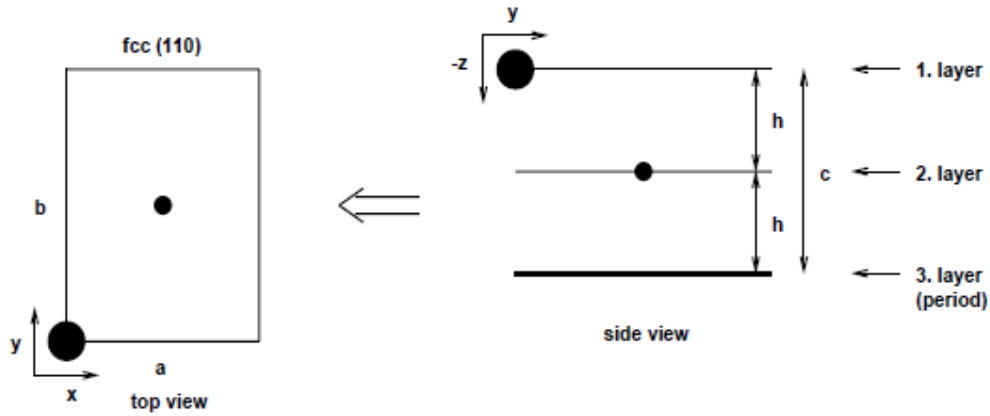


Figure 43: Unit cell to generate face centered (110) surface.

The relation between lattice constant ( $a_0$ ) and nearest neighbor distance ( $d_{nn}$ ) for the FCC crystal, the unit cell sizes in terms of lattice constant ( $a_0$ ), and the interlayer spacing ( $h$ ) are defined as

$$a_0 = \sqrt{2}d_{nn}, \quad a = \frac{1}{\sqrt{2}}a_0, \quad b = a_0, \quad c = \frac{1}{\sqrt{2}}a_0, \quad h = \frac{1}{2\sqrt{2}}a_0 \quad (23)$$

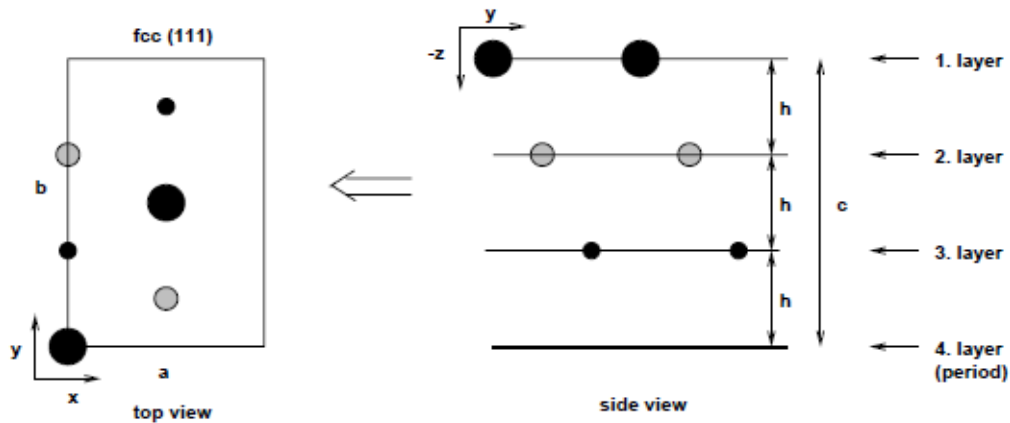


Figure 44: Unit cell to generate face centered (111) surface.

The relation between lattice constant ( $a_0$ ) and nearest neighbor distance ( $d_{nn}$ ) for the FCC crystal, the unit cell sizes in terms of lattice constant ( $a_0$ ), and the interlayer spacing ( $h$ ) are defined as

$$a_0 = \sqrt{2}d_{nn}, \quad a = \frac{1}{\sqrt{2}}a_0, \quad b = \sqrt{\frac{3}{2}}a_0, \quad c = \sqrt{3}a_0, \quad h = \frac{1}{\sqrt{3}}a_0 \quad (24)$$



## APPENDIX B

### C++ CUDA KERNEL CODE OF FORCE FUNCTION

```
#include "mdCuda.h"

__global__ void kernelForce(int NA, double* FFX, double* FFY, double* FFZ, double*
EE, double* X, double* Y, double* Z, int IPBC, double *Params)
{
    double XIJ, YIJ, ZIJ, RIJ, RIJ2, EPP, FX2, FY2, FZ2;
    double ARG1, ARG2, EXP1, EXP2, UIJ1, UIJ2, UIJ;
    double FAC1, FAC2, FAC12, XRIJ, YRIJ, ZRIJ;

    double PP0 = Params[0];
    double PP1 = Params[1];
    double PP2 = Params[2];
    double AL1 = Params[3];
    double AL2 = Params[4];
    double A1 = Params[5];
    double A2 = Params[6];
    double RL1 = Params[7];
    double RL2 = Params[8];
    double D21 = Params[9];
    double D22 = Params[10];

    int i = blockIdx.x * blockDim.x + threadIdx.x;

    EPP = 0;
    // Forces that effect atoms indexed with i in all three axes
    FX2 = 0;
    FY2 = 0;
    FZ2 = 0;

    for(int j=0; j<NA; j++)
    {
        if(i == j)
            continue;

        // Apply periodic boundaries and find distances between
        // atom i and j. RIJ2 is square of RIJ
        XIJ = X[i] - X[j];
        YIJ = Y[i] - Y[j];
        ZIJ = Z[i] - Z[j];

        double DD, ID;

        if(IPBC != 0){
            if(PP0 > 0){
                DD = XIJ / PP0;
                ID = int(DD);
                XIJ = XIJ - PP0*(ID+int(2.0*(DD-ID)));
            }
            if(PP1 > 0){
                DD = YIJ / PP1;
                ID = int(DD);
                YIJ = YIJ - PP1*(ID+int(2.0*(DD-ID)));
            }
        }
    }
}
```

```

    }
    if(PP2 > 0){
        DD = ZIJ / PP2;
        ID = int(DD);
        ZIJ = ZIJ - PP2*(ID+int(2.0*(DD-ID)));
    }
}
RIJ2 = XIJ*XIJ + YIJ*YIJ + ZIJ*ZIJ;
RIJ = sqrt(RIJ2);

// Calculate potential energy U(r)
ARG1 = AL1*RIJ2;
ARG2 = AL2*RIJ2;
EXP1 = exp(-ARG1);
EXP2 = exp(-ARG2);
UIJ1 = A1*EXP1/(pow(RIJ,RL1));
UIJ2 = A2*EXP2/(pow(RIJ,RL2));
UIJ = D21*UIJ1 + D22*UIJ2;
EPP = EPP+UIJ;

// Calculate forces
FAC1 = -(RL1/RIJ + 2.0*AL1*RIJ);
FAC2 = -(RL2/RIJ + 2.0*AL2*RIJ);
FAC12 = FAC1*D21*UIJ1 + FAC2*D22*UIJ2;
XRIJ = XIJ/RIJ;
YRIJ = YIJ/RIJ;
ZRIJ = ZIJ/RIJ;
FX2 += FAC12*XRIJ;
FY2 += FAC12*YRIJ;
FZ2 += FAC12*ZRIJ;
}

FFX[i] = -FX2;
FFY[i] = -FY2;
FFZ[i] = -FZ2;
EE[i] = EPP;
}

```

## APPENDIX C

### FORTRAN CODE OF PARALLEL FORCE FUNCTION

```
C =====
C SUBROUTINE FORCE
C =====
C CALCULATES FORCE COMPONENTS AND TOTAL FORCE FOR EACH PARTICLE
C =====
C IMPLICIT DOUBLE PRECISION (A-H,O-Z)
COMMON/CXYZ/ X(3000),Y(3000),Z(3000)
COMMON/CFOR/ FF(3000,3),FFF(3000),EE(3000)
COMMON/CENE/ EPOT,EKIN,ETOT,TEMP,SCFAC,TCALC,EKINA,TCALAV
COMMON/CPOT/ A1,A2,RL1,RL2,AL1,AL2,D21,D22
COMMON/CPAR/ RM,TE,BK,DT,NN,NA,IPD
COMMON/CSTP/ IAVL,MDSL,MDS,MDSC,ISCAL,IAVC,IPPL,MVTL,MVT
COMMON/CFOR/ RMD,RPD,RXX,DXX,PI2D
C =====
C E2=0.0D0
DO 10 I=1,NA
FF(I,1)=0.0D0
FF(I,2)=0.0D0
FF(I,3)=0.0D0
C FFF(I)=0.0D0
10 CONTINUE
C
!$OMP PARALLEL DO
!$OMP& PRIVATE(I,J,EPP,FX2,FY2,FZ2,RIJ,RIJ2,XIJ,YIJ,ZIJ,ARG1,ARG2,EXP1,
!$OMP& EXP2,UIJ1,UIJ2,UIJ,FAC1,FAC2,FAC12,XRIJ,YRIJ,ZRIJ)
!$OMP& REDUCTION(+:E2)
DO 40 I=1,NA
C
EE(I)=0.0D0
EPP=0.0D0
C Forces that effect atoms indexed with i in all three axes
FX2=0.0D0
FY2=0.0D0
FZ2=0.0D0
C
DO 30 J=1,NN
C IF(J.EQ.I) GO TO 30
C APPLY PERIODIC BOUNDARIES AND FIND DISTANCES BETWEEN ATOM I AND J. RIJ2 IS
SQUARE OF RIJ
CALL PERIOD(I,J,XIJ,YIJ,ZIJ,RIJ2,RIJ)
C
C Calculate U(r)
ARG1=AL1*RIJ2
ARG2=AL2*RIJ2
EXP1=DEXP(-ARG1)
EXP2=DEXP(-ARG2)
UIJ1=A1*EXP1/(RIJ**RL1)
UIJ2=A2*EXP2/(RIJ**RL2)
UIJ=D21*UIJ1+D22*UIJ2
E2=E2+UIJ
EPP=EPP+UIJ
```

```

C
C Calculate forces
FAC1=- (RL1/RIJ+2.0*AL1*RIJ)
FAC2=- (RL2/RIJ+2.0*AL2*RIJ)
FAC12=FAC1*D21*UIJ1+FAC2*D22*UIJ2
XRIJ=XIJ/RIJ
YRIJ=YIJ/RIJ
ZRIJ=ZIJ/RIJ
FX2=FX2+FAC12*XRIJ
FY2=FY2+FAC12*YRIJ
FZ2=FZ2+FAC12*ZRIJ
C
C 30 CONTINUE
C
FF (I, 1)=-FX2
FF (I, 2)=-FY2
FF (I, 3)=-FZ2
EE (I)=EPP
c FFF (I)=DSQRT (FF (I, 1) **2+FF (I, 2) **2+FF (I, 3) **2)
C
C 40 CONTINUE
!$OMP END PARALLEL DO
C
EPOT=E2
C
RETURN
END

```

# APPENDIX D

## SAMPLE INPUT AND OUTPUT FILES

### Input file for Au-111A

```
MOLECULAR-DYNAMICS SIMULATION FOR gold nanorod (111) medium PBC 300K
MDSL , IAVL, IPPL, ISCAL, IPD, TE , NA , LAYER, IPBC, PP(1), PP(2), PP(3)
15000000, 100 , 5000, 2 , 0 , 300.0 , 76 , 8 , 1 , 0.0 , 0.0 , 28.2672
(W(J,K),K=1,6), (NO(J,K),K=1,3)
2.885 , 0.0 , 0.0 , 2.885 , 4.997 , 7.0668 , 1 , 1 , 4
1.4425 , 2.4985 , 0.0 , 2.885 , 4.997 , 7.0668 , 2 , 1 , 4
1.4425 , 0.833 , 2.3556 , 2.885 , 4.997 , 7.0668 , 2 , 2 , 4
0.0 , 3.3313 , 2.3556 , 2.885 , 4.997 , 7.0668 , 3 , 1 , 4
0.0 , 1.666 , 4.7112 , 2.885 , 4.997 , 7.0668 , 3 , 1 , 4
1.4425 , 4.1641 , 4.7112 , 2.885 , 4.997 , 7.0668 , 2 , 1 , 4
0.0 , 4.997 , 0.0 , 2.885 , 4.997 , 7.0668 , 3 , 1 , 4
2.885 , 6.6626 , 4.7112 , 2.885 , 4.997 , 7.0668 , 1 , 1 , 4
```

### Part of output file for Au-100C

```
*****
MOLECULAR-DYNAMICS SIMULATION FOR gold nanorod (100) small PBC 300K
*****

DATE AND TIME: 2013.04.16 14:13:25

MDSL , IAVL, IPPL, ISCAL, IPD, TE , NA , LAYER, IPBC, PP(1), PP(2), PP(3)
2000000, 100 , 5000, 2 , 0 , 300.0 , 35 , 3 , 1 , 0.0 , 0.0 , 28.56

INITIAL COORDINATES:
2.04 , 0.0 , 2.04 , 4.08 , 4.08 , 4.08 , 1 , 2 , 7
0.0 , 2.04 , 2.04 , 4.08 , 4.08 , 4.08 , 2 , 1 , 7
2.04 , 2.04 , 0.0 , 4.08 , 4.08 , 4.08 , 1 , 1 , 7
*****

NUMBER OF MOVING ATOMS: NA= 35
NUMBER OF TOTAL ATOMS: NN= 35

INITIAL COORDINATES OF ALL ATOMS: (X,Y,Z)

1 2.04000 2.04000 0.00000
2 2.04000 4.08000 2.04000
3 0.00000 2.04000 2.04000
4 4.08000 2.04000 2.04000
5 2.04000 0.00000 2.04000
6 2.04000 2.04000 4.08000
7 2.04000 4.08000 6.12000
8 4.08000 2.04000 6.12000
9 2.04000 0.00000 6.12000
10 0.00000 2.04000 6.12000
11 2.04000 2.04000 8.16000
12 4.08000 2.04000 10.20000
13 0.00000 2.04000 10.20000
14 2.04000 0.00000 10.20000
15 2.04000 4.08000 10.20000
16 2.04000 2.04000 12.24000
17 2.04000 4.08000 14.28000
18 2.04000 0.00000 14.28000
19 0.00000 2.04000 14.28000
20 4.08000 2.04000 14.28000
21 2.04000 2.04000 16.32000
```

22	0.00000	2.04000	18.36000
23	2.04000	0.00000	18.36000
24	4.08000	2.04000	18.36000
25	2.04000	4.08000	18.36000
26	2.04000	2.04000	20.40000
27	2.04000	0.00000	22.44000
28	4.08000	2.04000	22.44000
29	0.00000	2.04000	22.44000
30	2.04000	4.08000	22.44000
31	2.04000	2.04000	24.48000
32	4.08000	2.04000	26.52000
33	2.04000	0.00000	26.52000
34	2.04000	4.08000	26.52000
35	0.00000	2.04000	26.52000

\*\*\*\*\*

INITIAL COORDINATES, FORCES AND ENERGIES:

I	X	Y	Z	FX	FY	FZ	EE
1	2.04000	2.04000	0.00000	-0.00000e+000	-0.00000e+000	4.88498e-015	-2.34171e+000
2	2.04000	4.08000	2.04000	-0.00000e+000	2.00690e-001	-4.11129e-016	-1.29303e+000
3	0.00000	2.04000	2.04000	-2.00690e-001	-0.00000e+000	-4.30211e-016	-1.29303e+000
4	4.08000	2.04000	2.04000	2.00690e-001	-0.00000e+000	-4.10262e-016	-1.29303e+000
5	2.04000	0.00000	2.04000	-0.00000e+000	-2.00690e-001	-4.14599e-016	-1.29303e+000
6	2.04000	2.04000	4.08000	-0.00000e+000	-0.00000e+000	-9.64940e-018	-2.34171e+000
7	2.04000	4.08000	6.12000	-0.00000e+000	2.00690e-001	1.37592e-016	-1.29303e+000
8	4.08000	2.04000	6.12000	2.00690e-001	-0.00000e+000	1.79226e-016	-1.29303e+000
9	2.04000	0.00000	6.12000	-0.00000e+000	-2.00690e-001	1.67516e-016	-1.29303e+000
10	0.00000	2.04000	6.12000	-2.00690e-001	-0.00000e+000	1.89634e-016	-1.29303e+000
11	2.04000	2.04000	8.16000	-0.00000e+000	-0.00000e+000	-5.21054e-015	-2.34171e+000
12	4.08000	2.04000	10.20000	2.00690e-001	-0.00000e+000	1.94837e-015	-1.29303e+000
13	0.00000	2.04000	10.20000	-2.00690e-001	-0.00000e+000	1.94425e-015	-1.29303e+000
14	2.04000	0.00000	10.20000	-0.00000e+000	-2.00690e-001	1.94490e-015	-1.29303e+000
15	2.04000	4.08000	10.20000	-0.00000e+000	2.00690e-001	1.95531e-015	-1.29303e+000
16	2.04000	2.04000	12.24000	-0.00000e+000	-0.00000e+000	1.47599e-017	-2.34171e+000
17	2.04000	4.08000	14.28000	-0.00000e+000	2.00690e-001	-1.70626e-015	-1.29303e+000
18	2.04000	0.00000	14.28000	-0.00000e+000	-2.00690e-001	-1.70713e-015	-1.29303e+000
19	0.00000	2.04000	14.28000	-2.00690e-001	-0.00000e+000	-1.71146e-015	-1.29303e+000
20	4.08000	2.04000	14.28000	2.00690e-001	-0.00000e+000	-1.69759e-015	-1.29303e+000
21	2.04000	2.04000	16.32000	-0.00000e+000	-0.00000e+000	3.06308e-016	-2.34171e+000
22	0.00000	2.04000	18.36000	-2.00690e-001	-0.00000e+000	-1.63405e-017	-1.29303e+000
23	2.04000	0.00000	18.36000	-0.00000e+000	-2.00690e-001	-1.72079e-017	-1.29303e+000
24	4.08000	2.04000	18.36000	2.00690e-001	-0.00000e+000	1.48846e-017	-1.29303e+000
25	2.04000	4.08000	18.36000	-0.00000e+000	2.00690e-001	3.04971e-017	-1.29303e+000
26	2.04000	2.04000	20.40000	-0.00000e+000	-0.00000e+000	-6.72964e-016	-2.34171e+000
27	2.04000	0.00000	22.44000	-0.00000e+000	-2.00690e-001	4.28997e-015	-1.29303e+000
28	4.08000	2.04000	22.44000	2.00690e-001	-0.00000e+000	4.29452e-015	-1.29303e+000
29	0.00000	2.04000	22.44000	-2.00690e-001	-0.00000e+000	4.27436e-015	-1.29303e+000
30	2.04000	4.08000	22.44000	-0.00000e+000	2.00690e-001	4.29344e-015	-1.29303e+000
31	2.04000	2.04000	24.48000	-0.00000e+000	-0.00000e+000	-1.97620e-014	-2.34171e+000
32	4.08000	2.04000	26.52000	2.00690e-001	-0.00000e+000	8.04912e-016	-1.29303e+000
33	2.04000	0.00000	26.52000	-0.00000e+000	-2.00690e-001	8.04912e-016	-1.29303e+000
34	2.04000	4.08000	26.52000	-0.00000e+000	2.00690e-001	8.04912e-016	-1.29303e+000
35	0.00000	2.04000	26.52000	-2.00690e-001	-0.00000e+000	8.18789e-016	-1.29303e+000

EPOT=-5.25969e+001 EKIN=3.44695e-002 TCALC=2.66667e+002 SCFAC=1.26795e+000

```

# ***** MD STEPS STARTED *****
#
# MDS      EPAV      EKAV      ETAV      TCALAV
#-----
#
100 -5.26761e+001 2.68440e+000 -4.99917e+001 2.98337e+002
200 -5.26751e+001 2.71485e+000 -4.99602e+001 3.00014e+002
300 -5.26739e+001 2.71482e+000 -4.99591e+001 3.00013e+002
400 -5.26694e+001 2.71516e+000 -4.99542e+001 3.00025e+002
500 -5.26707e+001 2.71474e+000 -4.99560e+001 3.00009e+002
600 -5.26632e+001 2.71489e+000 -4.99483e+001 3.00015e+002
700 -5.26693e+001 2.71451e+000 -4.99548e+001 3.00001e+002
800 -5.26623e+001 2.71424e+000 -4.99480e+001 2.99991e+002
900 -5.26705e+001 2.71428e+000 -4.99562e+001 2.99993e+002
1000 -5.26678e+001 2.71382e+000 -4.99539e+001 2.99976e+002
1100 -5.26738e+001 2.71414e+000 -4.99597e+001 2.99987e+002
1200 -5.26749e+001 2.71398e+000 -4.99609e+001 2.99982e+002
1300 -5.26774e+001 2.71428e+000 -4.99631e+001 2.99993e+002
1400 -5.26781e+001 2.71448e+000 -4.99636e+001 3.00000e+002
1500 -5.26776e+001 2.71474e+000 -4.99629e+001 3.00010e+002
1600 -5.26766e+001 2.71479e+000 -4.99618e+001 3.00012e+002
1700 -5.26730e+001 2.71512e+000 -4.99578e+001 3.00024e+002
1800 -5.26734e+001 2.71476e+000 -4.99586e+001 3.00010e+002
1900 -5.26666e+001 2.71497e+000 -4.99516e+001 3.00018e+002
2000 -5.26716e+001 2.71456e+000 -4.99570e+001 3.00003e+002
2100 -5.26644e+001 2.71438e+000 -4.99500e+001 2.99996e+002
2200 -5.26722e+001 2.71433e+000 -4.99578e+001 2.99994e+002
2300 -5.26686e+001 2.71388e+000 -4.99547e+001 2.99978e+002
2400 -5.26750e+001 2.71416e+000 -4.99609e+001 2.99988e+002
2500 -5.26756e+001 2.71392e+000 -4.99617e+001 2.99980e+002
2600 -5.26787e+001 2.71423e+000 -4.99645e+001 2.99991e+002
2700 -5.26798e+001 2.71437e+000 -4.99654e+001 2.99997e+002
2800 -5.26799e+001 2.71462e+000 -4.99653e+001 3.00006e+002
2900 -5.26791e+001 2.71475e+000 -4.99643e+001 3.00010e+002
3000 -5.26763e+001 2.71505e+000 -4.99613e+001 3.00021e+002
3100 -5.26760e+001 2.71479e+000 -4.99612e+001 3.00011e+002
3200 -5.26701e+001 2.71504e+000 -4.99550e+001 3.00020e+002
3300 -5.26738e+001 2.71461e+000 -4.99592e+001 3.00005e+002
3400 -5.26666e+001 2.71453e+000 -4.99521e+001 3.00001e+002

```

3500	-5.26738e+001	2.71438e+000	-4.99595e+001	2.99996e+002
3600	-5.26694e+001	2.71397e+000	-4.99554e+001	2.99981e+002
3700	-5.26762e+001	2.71419e+000	-4.99620e+001	2.99989e+002
3800	-5.26761e+001	2.71388e+000	-4.99622e+001	2.99978e+002
3900	-5.26802e+001	2.71420e+000	-4.99660e+001	2.99990e+002
4000	-5.26836e+001	2.71433e+000	-4.99693e+001	2.99995e+002
4100	-5.26954e+001	2.71486e+000	-4.99805e+001	3.00015e+002
4200	-5.27544e+001	2.71646e+000	-5.00379e+001	3.00073e+002
4300	-5.30516e+001	2.72408e+000	-5.03275e+001	3.00352e+002
4400	-5.43297e+001	2.74480e+000	-5.15849e+001	3.01113e+002
4500	-5.60149e+001	2.72624e+000	-5.32886e+001	3.00439e+002
4600	-5.57463e+001	2.70355e+000	-5.30428e+001	2.99598e+002
4700	-5.55224e+001	2.71638e+000	-5.28060e+001	3.00069e+002
4800	-5.54338e+001	2.71521e+000	-5.27186e+001	3.00024e+002
4900	-5.61539e+001	2.72678e+000	-5.34271e+001	3.00454e+002
5000	-5.59975e+001	2.70096e+000	-5.32966e+001	2.99502e+002

PERIODIC PRINTING OF COORDINATES, FORCES AND ENERGIES AT MDS: 5000

I	X	Y	Z	FX	FY	FZ	EE
1	9.32844	9.58497	8.35321	4.91480e-002	4.92920e-002	4.04808e-001	-2.06621e+000
2	10.25523	12.02117	10.00400	-3.17329e-001	-2.57751e-002	1.07142e+000	-1.46308e+000
3	8.44880	10.37739	11.58431	7.81089e-002	-1.07476e-001	-4.99634e-001	-1.41826e+000
4	12.18511	10.07911	9.69792	1.31073e-001	-3.83520e-001	-1.86325e-001	-1.44810e+000
5	10.27100	8.15732	10.79451	-1.69099e-001	9.49548e-002	-1.77170e-001	-1.25573e+000
6	11.20297	10.32520	12.37363	-1.49888e-001	-2.49013e-001	1.43727e-001	-2.19239e+000
7	10.71487	12.66718	13.77163	1.08518e-001	2.51631e-001	4.80938e-002	-1.27221e+000
8	12.97966	10.62216	14.57864	2.62097e-001	2.00352e-001	-1.41246e-001	-1.15118e+000
9	10.84795	8.79724	15.05404	1.75531e-001	-1.05498e-001	-1.00886e-001	-1.51151e+000
10	8.85859	10.58869	14.38325	-2.08807e-003	2.62295e-001	-6.94464e-003	-1.69293e+000
11	11.04149	11.50433	16.40386	-2.90618e-001	8.81492e-002	1.42637e-001	-2.13927e+000
12	12.47048	10.73818	19.34350	-2.64709e-001	1.21464e-001	-6.74894e-002	-1.34099e+000
13	8.32300	10.72773	17.18045	-1.20495e-001	-6.96338e-002	6.86609e-002	-1.30926e+000
14	10.59085	9.16323	17.89509	1.77237e-002	-2.52988e-001	2.75698e-002	-1.67218e+000
15	9.94388	12.13430	19.07117	1.32846e-001	-3.43543e-001	1.88685e-001	-1.66087e+000
16	9.65479	9.50023	20.54327	4.16605e-003	2.79309e-001	4.21648e-001	-1.87689e+000
17	10.02698	11.98246	22.04532	1.87271e-001	5.21491e-002	-1.73484e-001	-1.54604e+000
18	10.40774	8.11191	23.37599	-4.22412e-001	2.81704e-001	1.78603e-001	-1.38429e+000
19	8.23537	10.18316	23.33715	4.03103e-001	-2.69360e-001	1.02342e-001	-1.44163e+000
20	12.07029	9.94688	22.08660	1.76683e-001	2.70818e-001	5.91003e-002	-1.49290e+000
21	10.86453	10.89142	24.68755	-2.08762e-001	-3.94005e-001	-4.23970e-002	-2.25704e+000
22	8.40590	10.51359	26.32095	3.51167e-001	-8.89699e-002	-1.06057e-001	-1.49506e+000
23	10.51042	8.40035	26.34120	-1.14407e-001	2.90719e-001	-2.36508e-001	-1.51268e+000
24	12.55612	10.32980	27.10397	-3.97919e-001	1.36459e-001	2.73333e-001	-1.45616e+000
25	10.45133	12.45191	27.20031	7.60691e-002	-3.62703e-001	-1.57725e-002	-1.50340e+000
26	10.03400	9.96780	0.20235	1.42488e-001	1.73389e-001	1.36912e-001	-2.27969e+000
27	10.62406	8.75707	2.91029	-2.40019e-001	-3.28155e-002	-1.00980e-001	-1.54389e+000
28	12.59785	10.34435	1.66519	-2.29235e-001	3.87410e-001	-2.36786e-001	-1.35562e+000
29	8.56701	10.79789	2.74745	1.22444e-001	-1.60863e-001	2.62469e-003	-1.49809e+000
30	10.51976	12.53630	1.58026	2.84910e-001	-3.34680e-001	1.20961e-001	-1.44849e+000
31	10.96847	11.16303	4.47476	-2.36749e-001	1.71627e-002	-3.43569e-001	-2.01341e+000
32	11.74561	9.87125	6.89537	4.83690e-001	1.34680e-001	7.24301e-003	-1.55514e+000
33	9.95545	8.16820	5.64343	-2.69916e-001	-4.32627e-002	-2.21725e-002	-1.32403e+000
34	10.08965	12.15551	7.29941	6.07993e-002	1.48747e-001	-9.82609e-001	-1.42746e+000
35	8.34543	10.53177	5.66303	1.85811e-001	-1.65786e-002	4.16656e-002	-1.58232e+000

EPOT=-5.55884e+001 EKIN=2.71448e+000 TCALC=3.00000e+002 SCFAC=1.00194e+000



## APPENDIX E

### SIMULATION IMAGES OF COMPLETE STRAIN STEPS FOR CU-111A 300 K

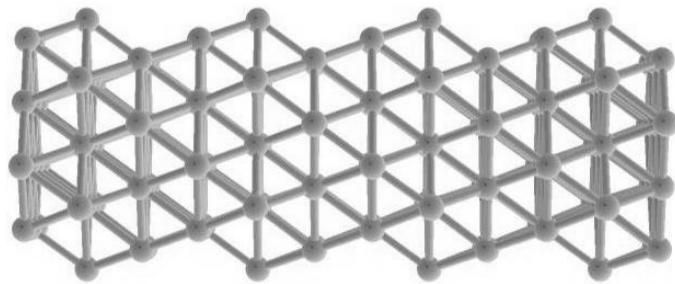


Figure 45: Initial structure of the nanowire.

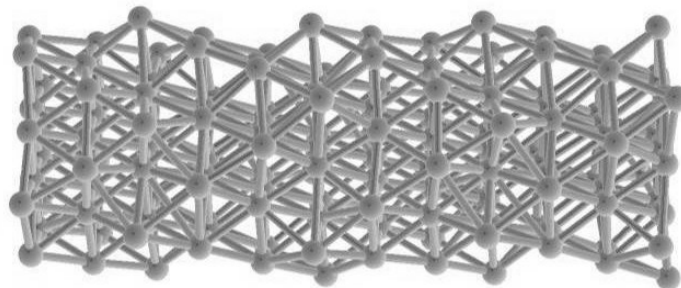


Figure 46: Relaxed structure of the nanowire.

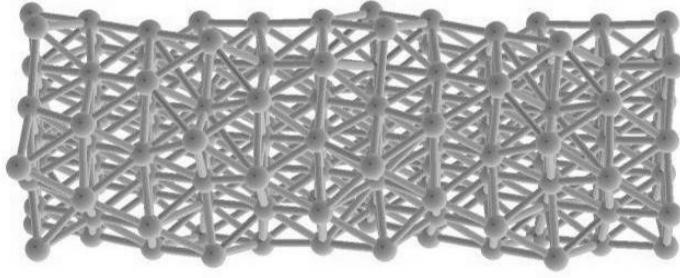


Figure 47: Relaxed structure of the nanowire after strain step 1.

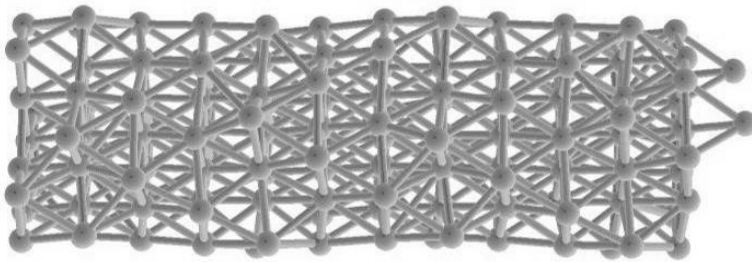


Figure 48: Relaxed structure of the nanowire after strain step 2.

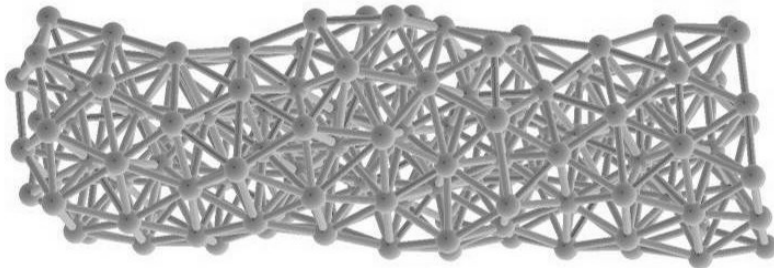


Figure 49: Relaxed structure of the nanowire after strain step 3.

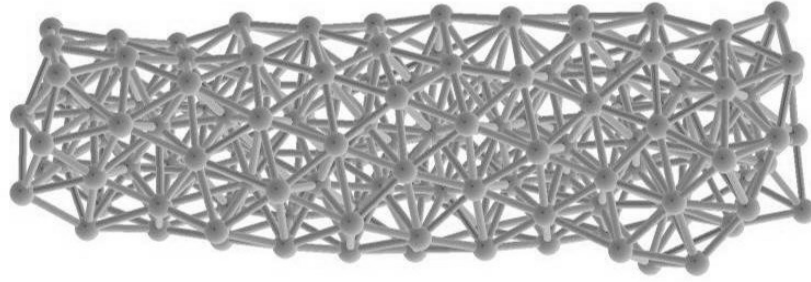


Figure 50: Relaxed structure of the nanowire after strain step 4.

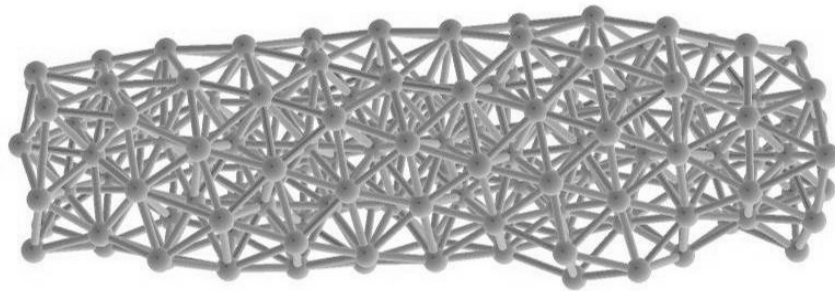


Figure 51: Relaxed structure of the nanowire after strain step 5.

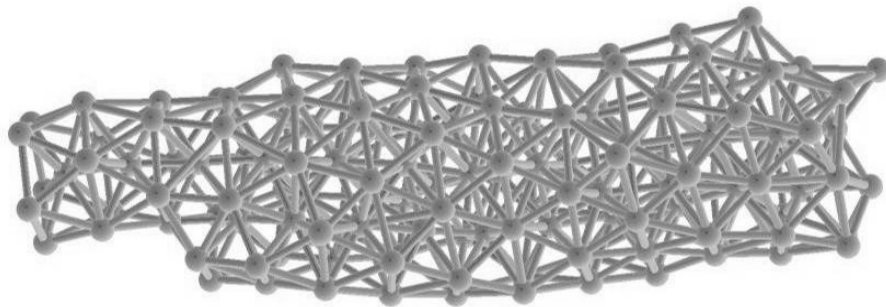


Figure 52: Relaxed structure of the nanowire after strain step 6.

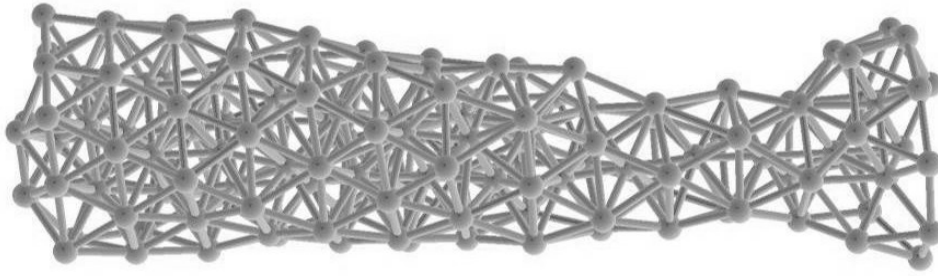


Figure 53: Relaxed structure of the nanowire after strain step 7.

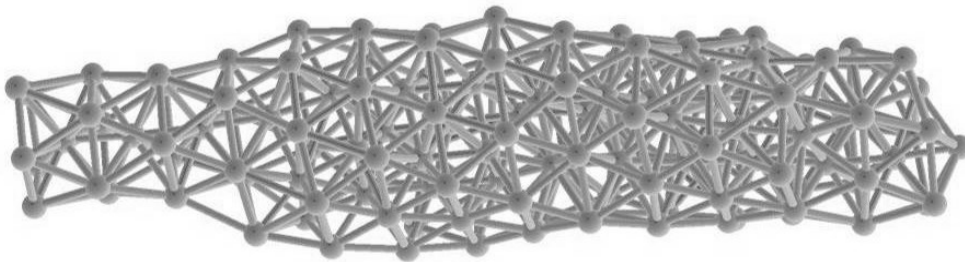


Figure 54: Relaxed structure of the nanowire after strain step 8.

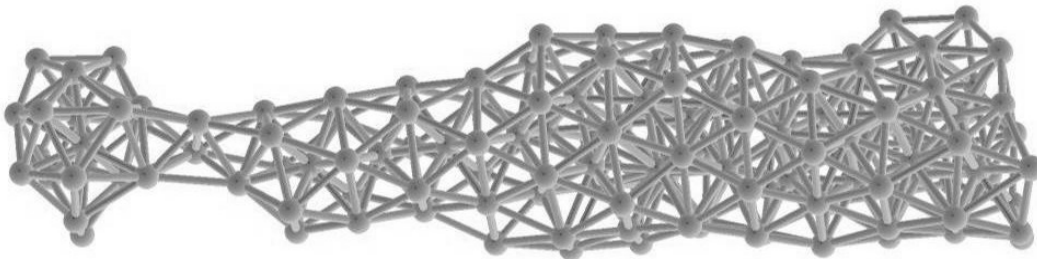


Figure 55: Relaxed structure of the nanowire after strain step 9.

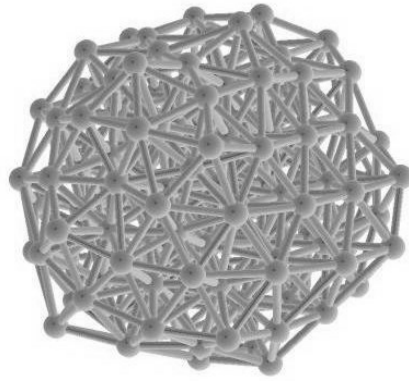


Figure 56: Relaxed structure of the nanowire after strain step 10. The nanowire has fragmented and clustered.